

# Simulating the $\text{H}_2$ content of high-redshift galaxies

Matteo Tomassetti <sup>\*</sup>, Cristiano Porciani, Emilio Romano-Díaz, Aaron D. Ludlow  
*Argelander Institut für Astronomie, Auf Dem Hügel 71, D-53121 Bonn, Germany*

Accepted 2014 October 28. Received 2014 October 20; in original form 2014 March 26

## ABSTRACT

We introduce a sub-grid model for the non-equilibrium abundance of molecular hydrogen in cosmological simulations of galaxy formation. We improve upon previous work by accounting for the unresolved structure of molecular clouds in a phenomenological way which combines both observational and numerical results on the properties of the turbulent interstellar medium. We apply the model to a cosmological simulation of the formation of a Milky Way-sized galaxy at  $z = 2$ , and compare the results to those obtained using other popular prescriptions that compute the equilibrium abundance of  $\text{H}_2$ . In these runs we introduce an explicit link between star formation and the local  $\text{H}_2$  abundance, and perform an additional simulation in which star formation is linked directly to the density of cold gas. In better agreement with observations, we find that the simulated galaxy produces less stars and harbours a larger gas reservoir when star formation is regulated by molecular hydrogen. In this case, the galaxy is composed of a younger stellar population as early star formation is inhibited in small, metal poor dark-matter haloes which cannot efficiently produce  $\text{H}_2$ . The number of luminous satellites orbiting within the virial radius of the galaxy at  $z = 2$  is reduced by 10–30 per cent in models with  $\text{H}_2$ -regulated star formation.

**Key words:** methods: numerical - ISM: molecules - galaxies: evolution - galaxies: formation

## 1 INTRODUCTION

The process of galaxy formation involves the interplay of many non-linear phenomena that span a wide range of length and time-scales. A galaxy like our Milky Way, for example, forms from a region that initially extends to roughly one comoving Mpc, yet its angular momentum is determined by the mass distribution within tens of comoving Mpc. Star formation (SF), on the other hand, takes place in the densest cores of giant molecular clouds (GMCs), on scales of the order of 0.1 pc.

The challenge in simulations of galaxy formation is to capture this vast dynamic range, while simultaneously accounting for the different physical processes that intervene on relevant scales. This is usually achieved with ad hoc sub-grid models that attempt to emulate the most important small-scale phenomena. In particular, one of the biggest uncertainties in simulations of galaxy formation is the means by which gas is converted into stars (see Dobbs et al. 2013, for a recent review).

The standard approach to this problem, motivated by observations, is to adopt a Schmidt-like law (Schmidt 1959), often coupled to conditions on the local gas properties. However, there are several issues with this method. First, its parameters are poorly constrained and are usually fine-tuned to match the observed Kennicutt-Schmidt (KS) relation (Kennicutt 1989, 1998). Secondly, there is a growing body of evidence that the local star formation rate (SFR) correlates more tightly with the observed density of molecular hydrogen than with that of the total gas density (e.g. Kennicutt et al. 2007; Bigiel et al. 2008; Leroy et al. 2008), though there is yet no consensus as to whether this reflects a causal relation. In particular, numerical simulations of isolated molecular clouds suggest that the presence of molecules does not boost the ability of the gas to cool and form stars (Glover & Clark 2012). The tight spatial correlation between  $\text{H}_2$  and young stars may then be due to the fact that they are both formed in high density regions where gas is effectively shielded from the interstellar radiation field.

Despite the ongoing debate, there are strong motivations for including a treatment of molecular hydrogen in cosmological simulations of galaxy formation. Observations of  $\text{H}_2$  proxies (such as CO luminosity), for example, have progressed tremendously over the past decade (see Carilli & Walter 2013, for a recent review), underlining the need for

<sup>\*</sup> E-mail: mtomas@astro.uni-bonn.de  
Member of the International Max Planck Research School (IMPRS) for Astronomy and Astrophysics at the Universities of Bonn and Cologne

robust theoretical templates to aid in the design of observational campaigns and the interpretation of their results. Furthermore, numerical simulations constitute a unique tool to test the impact of H<sub>2</sub>-regulated SF on the global structure of galaxies, provided their H<sub>2</sub> content can be reliably determined.

Tracking H<sub>2</sub>, however, requires solving a challenging network of rate equations which are coupled to a radiative-transfer computation for H<sub>2</sub>-dissociating photons. Given that the spatial resolution of current simulations is comparable in size to GMCs, these calculations must be done at the sub-grid level and include a description of gas structure on the unresolved scales (e.g. a clumping factor for the gas density).

Recently, several authors have incorporated simple algorithms to track molecular hydrogen in hydrodynamical simulations of galaxy formation. For instance, Pelupessy et al. (2006) monitored the H<sub>2</sub> distribution in dwarf-sized galaxies within a fixed dark matter (DM) potential and showed that the resulting molecular mass depends strongly on the metallicity of the interstellar medium (ISM). Similar conclusions were drawn by Gnedin et al. (2009, see also Feldmann et al. (2011)), who followed the evolution of the H<sub>2</sub> content for 100 Myr in a cosmologically simulated galaxy at  $z = 4$ . These authors showed that it is only possible to form fully shielded molecular clouds when the gas metallicity is high (i.e.  $Z \sim 10^{-2} - 10^{-1} Z_{\odot}$ ), and argued that H<sub>2</sub>-regulated SF can act as an effective feedback mechanism, delaying SF in the low-metallicity progenitors of a galaxy.

The implications of these results for galaxy formation in low-mass haloes were studied further by Kuhlen et al. (2012, 2013), who suggested the possible existence of a large population of low-mass, gas-rich galaxies that never reached the critical column density required for the H<sub>2</sub>/HI transition and are thus devoid of stars. Their work, however, was based on an analytic model for H<sub>2</sub> formation that assumes chemical equilibrium between its formation and destruction rates (Krumholz et al. 2008, 2009; McKee & Krumholz 2010). None the less, Krumholz & Gnedin (2011) showed that this model agrees well with a time-dependent solution to the chemical network provided the local metallicity of the gas is above  $10^{-2} Z_{\odot}$ , lending support to these conclusions.

Christensen et al. (2012) modelled the non-equilibrium abundance of H<sub>2</sub> in a dwarf galaxy that was simulated down to redshift  $z = 0$ , connecting SF explicitly to the local H<sub>2</sub> content of the gas. These authors showed that, compared to simulations rooted on the Schmidt law, molecule-based SF produces a galaxy which is more gas rich, has bluer stellar populations and a clumpier ISM. On the other hand, strong stellar feedback, when included, tends to mitigate these differences by regulating the formation and destruction rates of GMCs (Hopkins et al. 2012).

In this paper, we introduce a new time-dependent sub-grid model for tracking the non-equilibrium abundance of H<sub>2</sub> in cosmological simulations of galaxy assembly. Our approach builds upon the work of Gnedin et al. (2009) and Christensen et al. (2012) by including additional information on the unresolved distribution of gas temperatures and densities. In particular, our model: (i) explicitly accounts for the distribution of sub-grid densities, as determined by observations and numerical simulations of turbulent GMCs; (ii) invokes a gas temperature-density relation that was de-

termined from detailed numerical studies of the ISM (Glover & Mac Low 2007a); and (iii) consistently takes into account that denser, unresolved clumps have larger optical depths.

As an application, we employ the model in a high-resolution simulation that follows the formation of a Milky Way-sized galaxy down to  $z = 2$ . In order to explore the interplay between SF, H<sub>2</sub> abundance and galactic structure, we re-simulate the same volume using different algorithms for computing the density of molecular hydrogen and the local SFR.

This paper is organized as follows. In Section 2, we introduce our model for tracking the non-equilibrium H<sub>2</sub> abundance and compare it with other commonly adopted prescriptions that have been discussed in the literature. In Sections 3 and 4, we describe our suite of simulations and present our main results. Finally, we summarize our main conclusions and then critically discuss some of our assumptions in Section 5.

## 2 MOLECULAR HYDROGEN

The abundance of molecular hydrogen in the metal-rich ISM is mainly regulated by the competition between its formation due to the catalytic action of dust grains and its photo-dissociation via the two-step Solomon process. In the ground state, H<sub>2</sub> absorbs electromagnetic radiation in two densely packed series of lines (the Lyman band – characterized by photon energies  $E > 11.2$  eV or wavelengths  $\lambda < 1108$  Å – and the Werner band –  $E > 12.3$  eV,  $\lambda < 1008$  Å). Radiative decay from the excited states leads to dissociation in approximately 15 per cent of the cases. Direct photo-dissociation would require photons with energy  $E > 14.7$  eV, but these are principally absorbed by hydrogen atoms as they lie above the hydrogen photo-ionization threshold (13.6 eV, 912 Å). As a result, only photons between  $912 \text{ \AA} < \lambda < 1108 \text{ \AA}$  can photo-dissociate molecular hydrogen.

Lyman-Werner (LW) photons are copiously emitted by OB stars, but intervening H<sub>2</sub> and dust effectively shield the densest regions of the ISM. This results in an H<sub>2</sub> abundance that increases rapidly towards regions in which the medium becomes optically thick to LW radiation.

An exact treatment of these effects is challenging: it requires three-dimensional radiative transfer calculations capable of resolving length and time-scales orders of magnitude shorter than those associated with galaxy evolution. Nevertheless, it is possible to follow the formation of molecular complexes in a phenomenological way, using approximate sub-grid treatments of the most crucial physical processes involved.

In this work, we use three different mathematical models that attempt to approximate these effects. The simplest (KMT-EQ) is fully analytical; it returns the equilibrium H<sub>2</sub> fraction in terms of quantities that can be determined locally in a simulation (Krumholz et al. 2008, 2009; McKee & Krumholz 2010). The model is based on a spherical molecular complex immersed in an isotropic bath of LW photons. Assuming that the ISM is in a two-phase equilibrium between a cold and a warm neutral medium, it allows both the intensity of the radiation field and the resulting H<sub>2</sub> fraction to be expressed in terms of the local gas column density and metallicity (Krumholz & Gnedin 2011).

The second model (KMT-UV) employs the same analytical relation between the equilibrium H<sub>2</sub> fraction and the radiation density in the LW band. However, in this case, the latter is calculated numerically within the simulations themselves. This is achieved by propagating photons from stellar particles assuming that the ISM is optically thin within a characteristic length scale and optically thick beyond that (see Appendix A for further details).

Note, however, that the formation of molecular hydrogen on dust grains is a very inefficient process. In the metal poor ISM, for example, the H<sub>2</sub> formation time-scale approaches a Hubble time. This calls into question the appropriateness of the equilibrium-based models, which *instantaneously* populate each simulation volume element with a given fraction of H<sub>2</sub>. This has motivated several authors (Pelupessy et al. 2006; Gnedin et al. 2009; Christensen et al. 2012) to develop more sophisticated algorithms capable of tracking the non-equilibrium H<sub>2</sub> fraction in high-resolution simulations. Inspired by these efforts, we have developed a novel dynamical model (DYN) for calculating the abundance of molecular hydrogen. This model is described in detail in the following subsection.

## 2.1 Mathematical formulation of the model

The evolution of the H<sub>2</sub> number density is described by the following system of equations:

$$\frac{dn_{\text{H}_2}}{dt} = \mathcal{R}_f(T) n_{\text{HI}} n_{\text{H}} - G \kappa \Phi e^{-\tau} n_{\text{H}_2} - \gamma_{\text{HI}} n_{\text{HI}} n_{\text{H}_2} - \gamma_{\text{H}_2} n_{\text{H}_2}^2, \quad (1)$$

$$\frac{dn_{\text{HI}}}{dt} = n_e n_{\text{HII}} k_1(T) - n_{\text{HI}} [k_2(T) n_e + \Gamma(z)] - 2 \frac{dn_{\text{H}_2}}{dt}, \quad (2)$$

$$n_{\text{HI}} + n_{\text{HII}} + 2n_{\text{H}_2} = n_{\text{H}}. \quad (3)$$

Here  $n_{\text{HI}}$ ,  $n_{\text{HII}}$  and  $n_{\text{H}_2}$  are, respectively, the number densities of neutral, ionized and molecular hydrogen;  $n_e$  is the electron number density;  $\gamma_i$  is the H<sub>2</sub> collisional destruction rate due to interaction with species  $i$ ;  $G$  is the unshielded interstellar UV-radiation flux in Habing units (see Appendix A);  $\kappa$  is the H<sub>2</sub> photo-dissociation rate for  $G = 1$ ;  $\Gamma(z)$  is the photo-ionization rate<sup>1</sup> of HI;  $k_1$  and  $k_2$  are the hydrogen recombination and collisional destruction rates;  $\tau = \sigma_d N_{\text{H}}$  is the optical depth of dust in the LW bands (conventionally evaluated at 1000 Å), where  $N_{\text{H}}$  is the total hydrogen column density. This assumes that the dust abundance scales linearly with the gas metallicity and the dust-to-gas mass ratio is equal to the value measured in the Milky Way (MW), i.e.  $10^{-2} Z/Z_{\odot}$ . The parametrization of the H<sub>2</sub> self-shielding function,  $\Phi$  (approximated for the plane parallel case) and the H<sub>2</sub> formation rate on dust grains,  $\mathcal{R}_f$ , are given in Table 1, and adopt a dust temperature  $T_d = 10$  K.

<sup>1</sup> In terms of the UV-background intensity,  $J_{\nu}$ , the ionization cross-section  $\sigma$  and the corresponding optical depth  $\tau'$ ,  $\Gamma(z) = \int_{\nu_0}^{+\infty} 4\pi J(\nu, z) \sigma(\nu) e^{-\tau'(\nu)} / (h_{\text{p}} \nu) d\nu$ , where  $\nu_0 = 13.6 \text{ eV}/h_{\text{p}}$  and  $h_{\text{p}}$  denotes the Planck constant.

### 2.1.1 Accounting for unresolved structures

Cosmological simulations of galaxy formation are limited in spatial resolution, and even the highest resolution runs employ computational elements that extend for only a few tens of parsecs. Observations and numerical studies of the turbulent ISM, on the other hand, reveal a complex gas density distribution on much smaller scales, consisting of filamentary structures and clumps (e.g. Glover & Mac Low 2007a). This structure is normally approximated in cosmological simulations by introducing a density clumping factor,  $C_{\rho}$ . However, as already noted by Micic et al. (2012), this does not take into account the full distribution of sub-grid densities, nor the effective density-temperature relation, both of which may modify the sub-grid H<sub>2</sub> formation and destruction rates.

Motivated by observations of the GMC density distribution (e.g. Kainulainen et al. 2009; Schneider et al. 2013), we assume that sub-grid clumps follow a lognormal (mass-weighted) probability density function (PDF):

$$\mathcal{P}_{\text{M}} dn_{\text{H}} = \frac{1}{\sqrt{2\pi\sigma n_{\text{H}}}} e^{-\frac{(\ln n_{\text{H}} - \mu)^2}{2\sigma^2}} dn_{\text{H}}, \quad (4)$$

where  $\mu$  and  $\sigma$  are parameters that can be determined once a clumping factor has been chosen. To do so, note that the average hydrogen density within a computational volume element,  $\langle n_{\text{H}} \rangle$ , is simply the integral over the volume-weighted sub-grid density PDF,  $\mathcal{P}_{\text{V}}$ :

$$\langle n_{\text{H}} \rangle = \frac{\int_0^{\infty} dn_{\text{H}} n_{\text{H}} \mathcal{P}_{\text{V}}}{\int_0^{\infty} dn_{\text{H}} \mathcal{P}_{\text{V}}} = e^{\mu - \sigma^2/2}, \quad (5)$$

where the last expression derives from the fact that  $\mathcal{P}_{\text{V}}/\mathcal{P}_{\text{M}} = \langle n_{\text{H}} \rangle/n_{\text{H}}$ . Similarly,  $C_{\rho} \equiv \langle n_{\text{H}}^2 \rangle / \langle n_{\text{H}} \rangle^2 = e^{\sigma^2}$ , so that the sub-grid density PDF is fully determined by  $C_{\rho}$  and the total hydrogen density in a cell.

In principle,  $C_{\rho}$  is a local variable whose value depends on the turbulent velocity dispersion of the ISM (e.g. Price et al. 2011). However, for simplicity, and in order to facilitate comparison with previous work, we set  $C_{\rho} = 10$  which has been shown to reproduce observed H<sub>2</sub> fractions in nearby galaxies (e.g. Gnedin et al. 2009; Christensen et al. 2012).

We assume that unresolved gas concentrations follow a temperature-density relation that emerges from simulations of the turbulent ISM (see Figure 17 in Glover & Mac Low 2007b). These results suggest that, at the densities relevant for efficient H<sub>2</sub> formation, gas temperatures rarely exceed 200 K. We therefore assume that atomic hydrogen and helium remain neutral within each cell, and neglect the collisional terms in equations (1) and (2). The resulting equations can then be rewritten as

$$\frac{d\langle n_{\text{H}_2} \rangle}{dt} = \langle \mathcal{R}_f(T) n_{\text{HI}} n_{\text{H}} \rangle - \langle G \kappa \Phi e^{-\tau} n_{\text{H}_2} \rangle, \quad (6)$$

$$\frac{d\langle n_{\text{HI}} \rangle}{dt} = -2 \frac{d\langle n_{\text{H}_2} \rangle}{dt}, \quad (7)$$

$$\langle n_{\text{HI}} \rangle + 2\langle n_{\text{H}_2} \rangle = \langle n_{\text{H}} \rangle. \quad (8)$$

### 2.1.2 Solving the differential equations

Given our assumptions for the sub-grid density and temperature distributions, the above rate equations are exact. However, it is impractical to preserve the information about the abundance of molecular hydrogen at each sub-grid

Parameter	Symbol	Expression	Reference
Clumping factor	$C_\rho$	$\langle n_{\text{H}}^2 \rangle / \langle n_{\text{H}} \rangle^2 = 10$	1,2
H <sub>2</sub> formation rate on dust grains	$\mathcal{R}_f(T)$	$3.025 \times 10^{-17} S_{\text{H}}(T) (T/100 \text{ K})^{0.5} (Z/Z_\odot)$	5,6
Sticking probability for H atoms	$S_{\text{H}}(T)$	$\left[ 1 + 0.4 \left( \frac{T+T_d}{100 \text{ K}} \right)^{1/2} + 0.2 \left( \frac{T}{100 \text{ K}} \right) + 0.08 \left( \frac{T}{100 \text{ K}} \right)^2 \right]^{-1}$ , $T_d = 10 \text{ K}$	3,4
H <sub>2</sub> photo-dissociation rate	$\kappa$	$4.2 \times 10^{-11} \text{ s}^{-1}$	7
Self-shielding function	$\Phi$	$\frac{1-\omega}{(1+x/b_5)^2} + \frac{\omega}{(1+x)^{1/2}} \exp[-8.5 \times 10^{-4}(1+x)^{1/2}]$ $x = N_{\text{H}_2}/5 \times 10^{14} \text{ cm}^{-2}$ , $\omega = 0.035$ , $b_5 = 2$	7,8
Cross-section at 1000 Å	$\sigma_d$	$2 \times 10^{-21} (Z/Z_\odot) \text{ cm}^2$	7

References:

1: Gnedin et al. (2009) 2: Christensen et al. (2012), 3: Cazaux & Spaans (2009), 4: Burke & Hollenbach (1983), 5: Tielens & Hollenbach (1985), 6: Cazaux & Spaans (2004), 7: Draine & Bertoldi (1996) 8: Sternberg et al. (2014)

**Table 1.** Parameters of the non-equilibrium model for the H<sub>2</sub> abundance.

density between time steps, and further simplifications are needed. We therefore assume that, within a computational cell, atomic gas transitions to a fully molecular state above a critical (sub-grid) density threshold,  $n_c$ . With this, equation (6) reduces to

$$\frac{d\langle n_{\text{H}_2} \rangle}{dt} = \langle n_{\text{H}} \rangle \left( \int_0^{n_c} dn \mathcal{R}_f[T(n)] n \mathcal{P}_{\text{M}} - \frac{\langle G \rangle \kappa}{2} \int_{n_c}^{+\infty} dn \Phi(n) e^{-\tau(n)} \mathcal{P}_{\text{M}} \right). \quad (9)$$

Note that, for a lognormal probability distribution of densities,  $n_c$  can be obtained solving for the root of

$$\langle n_{\text{H}_2} \rangle = \frac{\langle n_{\text{H}} \rangle}{4} \left[ 1 + \text{Erf} \left( \frac{\mu - \ln(n_c)}{\sqrt{2}\sigma} \right) \right]. \quad (10)$$

At each time step of the simulation, we solve equation (9) in relevant cells using a variable step-size, variable order, implicit integrator. Using this we determine the *total* H<sub>2</sub> density per cell, which we advect with the gas flow at each timestep.

### 2.1.3 Estimating optical depths

In order to evaluate equation (9), the H and H<sub>2</sub> column density (which are necessary to compute the dust optical depth,  $\tau(n)$ , and the self-shielding function,  $\Phi$ , respectively) must be specified. A common choice is to compute column densities (surface densities in case of the KMT model) by means of a Sobolev-like approximation

$$N_{\text{H}} \approx \langle n_{\text{H}} \rangle \times l_{\text{sob}}, \quad \Sigma_{\text{gas}} \approx \langle \rho_{\text{gas}} \rangle \times l_{\text{sob}}, \quad (11)$$

where  $l_{\text{sob}} = \langle n_{\text{H}} \rangle / |\nabla \langle n_{\text{H}} \rangle|$ , and  $\rho_{\text{gas}}$  is the total gas density. This is a reasonable approximation in simulations where computational elements are of comparable extension to the sizes of GMCs (Gnedin et al. 2009; Christensen et al. 2012; Kuhlen et al. 2012). However, because H<sub>2</sub> self-shielding takes place in narrow lines, equation (11) may over-estimate the H<sub>2</sub> column density by a large factor. For this reason, Gnedin & Kravtsov (2011) compute  $N_{\text{H}_2}$  using the product between the H<sub>2</sub> volume density and a fixed characteristic length,  $L_c \simeq C_\rho 10 \text{ pc}$ , which is tuned to match observations of the H<sub>2</sub> fraction as a function of  $N_{\text{H}}$ . In our model, we compute the column densities of atomic and molecular hydrogen consistently with equation (4) by simply assuming that

the sub-grid density distribution is plane-parallel. Although this highly symmetric configuration cannot exactly hold in a turbulent medium, it provides a reasonable estimate of the relation between volume and column densities and is often used in the literature of molecular clouds (e.g. Tielens & Hollenbach 1985; Sternberg et al. 2014, and references therein). In this case, the total hydrogen mass associated with sub-grid densities below  $n_{\text{H}}$  is related to the hydrogen column density:

$$\int_0^{n_{\text{H}}} dn'_{\text{H}} \mathcal{P}_{\text{M}}(n'_{\text{H}}) = \frac{1}{\langle n_{\text{H}} \rangle \Delta x} \int_0^z dz' n_{\text{H}}. \quad (12)$$

Therefore, the final expressions for the column densities are

$$N_{\text{H}}(n_{\text{H}}) = \frac{\langle n_{\text{H}} \rangle \Delta x}{2} \left[ 1 - \text{Erf} \left( \frac{\mu - \ln(n_{\text{H}})}{\sqrt{2}\sigma} \right) \right] \quad (13)$$

$$N_{\text{H}_2}(n_{\text{H}}) = \frac{\langle n_{\text{H}} \rangle \Delta x}{4} \left[ \text{Erf} \left( \frac{\mu - \ln(n_c)}{\sqrt{2}\sigma} \right) - \text{Erf} \left( \frac{\mu - \ln(n_{\text{H}})}{\sqrt{2}\sigma} \right) \right]. \quad (14)$$

As we will show in Section 4.3, our model accurately reproduces the observed relation between the H<sub>2</sub> fraction and the column density of neutral hydrogen without introducing additional free parameters.

### 2.1.4 Example solutions

To develop an intuitive understanding of the impact of our sub-grid density distribution on H<sub>2</sub> formation, we integrate the rate equations for 500 Myr and compute the H<sub>2</sub> content for cells of fixed density and metallicity in a constant UV field. The results are shown in Figure 1, where curves correspond to  $\langle f_{\text{H}_2} \rangle = 2\langle n_{\text{H}_2} \rangle / \langle n_{\text{H}} \rangle = 0.5$  in the  $(\langle n_{\text{H}} \rangle, \langle G \rangle)$  plane for gas metallicities ranging from  $10^{-3}$  to  $10 Z_\odot$ . As expected, higher metallicity gas forms H<sub>2</sub> more efficiently at low densities. This is due to the enhanced rate of H<sub>2</sub> formation on dust grains, but also to the increased optical depth to LW photons (see equations (13) and (14)). More importantly, note that the H<sub>2</sub> fraction is nearly independent of  $\langle G \rangle$ , suggesting that our results will not be strongly influenced by our treatment of the UV field.

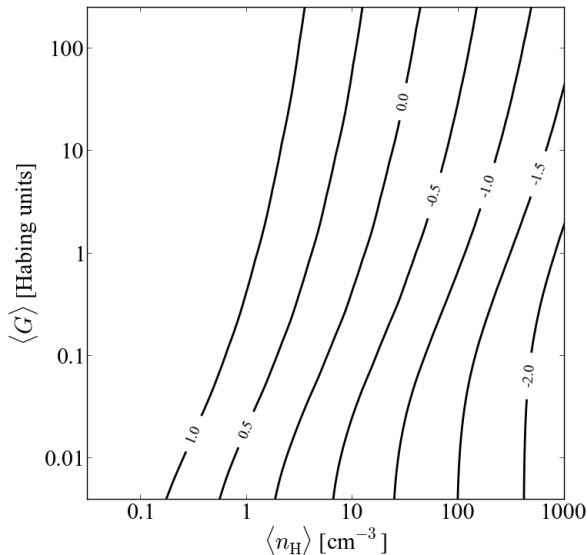


**Figure 1.** Lines of constant  $\langle f_{H_2} \rangle = 0.5$  as a function of the total hydrogen density,  $\langle n_H \rangle$ , and the interstellar UV field,  $\langle G \rangle$ , for the DYN model after an integration time of 500 Myr. Labels along each curve indicate the logarithm of the gas metallicity in solar units.

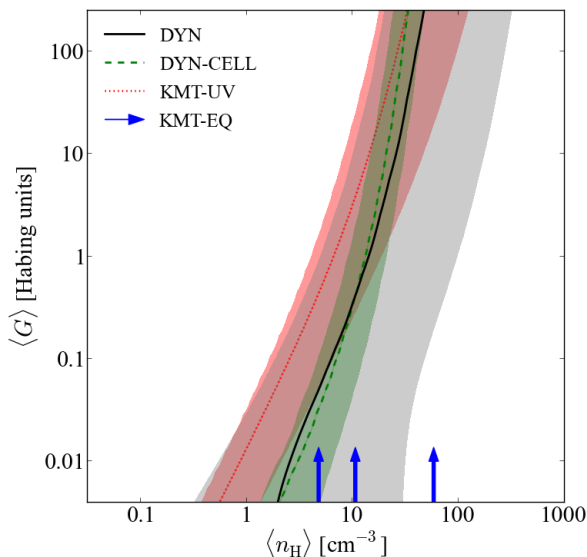


**Figure 2.** Lines correspond to contours of  $\langle f_{H_2} \rangle = 0.5$  for a solar metallicity gas. Different linestyles correspond to the different  $H_2$  formation models described in Section 2, as indicated in the legend. The dashed (green) line, labelled DYN-CELL, shows the results of the DYN model in which sub-grid densities are accounted for using a clumping factor rather than a sub-grid density PDF. Shaded regions of similar colour highlight the zone  $0.1 < \langle f_{H_2} \rangle < 0.9$  for each model. Upward pointing arrows mark  $\langle f_{H_2} \rangle = 0.1, 0.5$  and  $0.9$  (from left to right) for KMT-EQ, which is independent of  $\langle G \rangle$ . For the non-equilibrium models, the solution has been computed after a total integration time of 500 Myr.

## 2.2 A Comparison of $H_2$ Formation Models

In Figure 2 we compare the predictions of the three  $H_2$ -formation models described above (KMT-EQ, KMT-UV and DYN). Lines show contours of  $\langle f_{H_2} \rangle = 0.5$  in the plane of UV field and gas density for a solar metallicity gas; shaded regions indicate the range  $0.1 < \langle f_{H_2} \rangle < 0.9$ . Different line styles correspond to the different models: DYN (solid), KMT-UV (dotted), and upward pointing arrows mark  $\langle f_{H_2} \rangle = 0.1, 0.5$  and  $0.9$  (from left to right) for KMT-EQ (which, by construction, is independent of  $\langle G \rangle$ ).

We also show, using a dashed (green) line, the time-dependent solution obtained after multiplying all quadratic terms by  $C_\rho = 10$  but without integrating over the sub-grid density PDF. This approximation (labelled DYN-CELL) has been used in previous work (Gnedin et al. 2009; Christensen et al. 2012), and is shown here for comparison. In this case, we set a constant gas temperature of  $T = 10^3$  K, which is typical of star-forming cells in simulations of galaxy formation, and compute the  $H_2$  column density as  $\langle n_{H_2} \rangle L_c$ , with  $L_c = 1$  pc (e.g. Gnedin & Kravtsov 2011). The solutions for all time-dependent models have been integrated for 500 Myr. Note that within this time, a dynamical equilibrium between  $H_2$  formation on dust grains and photo-dissociation due to interstellar radiation has been reached at gas densities  $\langle n_H \rangle \gtrsim 1$   $\text{cm}^{-3}$  and a longer integration time would only impact the very low density regions, without altering our conclusions.

It is worth noting that the DYN and DYN-CELL models have very similar contours at  $\langle f_{H_2} \rangle = 0.5$  over roughly five orders of magnitude in UV field. The  $\langle f_{H_2} \rangle = 0.1$  and  $0.9$  contours, on the other hand, differ dramatically. For example, for  $\langle G \rangle = 1$ , the DYN model predicts an  $H_2$  fraction of  $0.9$  at  $\langle n_H \rangle \sim 100$   $\text{cm}^{-3}$ , while in the DYN-CELL model the same  $H_2$  fraction is obtained at a density which is approximately 10 times lower. This results from the sub-grid temperature-density relation in the DYN model: dense clumps, in this case, are very cold, which inhibits the efficient formation of  $H_2$  on dust grains. For example, at  $\langle n_H \rangle \gtrsim 10^2$   $\text{cm}^{-3}$  sub-grid clumps have  $T \lesssim 10^2$  K. Since the  $H_2$  formation rate,  $\mathcal{R}_f$ , is proportional to  $\sqrt{T} S_H(T)$ , this results in lower  $\langle f_{H_2} \rangle$  than for the DYN-CELL model, where  $T = 10^3$  K everywhere.

However, for the same value of  $\langle G \rangle$ ,  $\langle f_{H_2} \rangle = 0.1$  is reached at much lower densities in the DYN model. In this regime, the temperature does not strongly affect the  $H_2$  formation rate. The difference, in this case, is due to the integration over the sub-grid densities, which enhances shielding from LW photons resulting in higher  $H_2$  abundances.

At equilibrium, the predictions of the DYN model are consistent with those of the KMT-UV and KMT-EQ models, but the impact of a time-dependent  $H_2$  chemistry may be affected by differing treatments of  $H_2$  formation on sub-grid scales. In order to test the impact of these assumptions, we have used each model described above to simulate the formation of a massive galaxy at  $z = 2$ . These simulations are described below.

Run	H <sub>2</sub> model	$\dot{\rho}_{\text{SF}} \propto \langle \rho_i \rangle$	SNe destroy H <sub>2</sub>	$\ell_i$	$\ell_f$	$\Delta x$ (pc)	$z_i$	$z_f$
STD	KMT-UV	gas	-	11	17	180	99	2
DYN	DYN	H <sub>2</sub>	-	11	17	180	99	2
DYN-SNe	DYN	H <sub>2</sub>	✓	11	17	180	99	2
KMT-EQ	KMT-EQ	H <sub>2</sub>	-	11	17	180	99	2
KMT-UV	KMT-UV	H <sub>2</sub>	-	11	17	180	99	2

**Table 2.** Main parameters of the simulations used in this work. Four sub-grid models of increasing complexity have been employed to compute the H<sub>2</sub> density. In the simplest case, KMT-EQ, the chemical-equilibrium abundance of molecular hydrogen is computed assuming that the ISM consists of a cold and a warm phase as in Krumholz et al. (2008). A variant of this technique, in which the flux of LW photons is computed explicitly by propagating radiation from the stars in the simulation forms the KMT-UV algorithm. Finally, the DYN model returns the non-equilibrium H<sub>2</sub> density and takes into account unresolved overdensities as described in Section 2.1. A slightly modified method is adopted in the DYN-SNe simulation in which SNa feedback destroys H<sub>2</sub>. In all the simulations, stars are formed proportionally to the density of molecular hydrogen with the exception of the STD run in which SF scales as the density of cold gas. The meaning of symbols is as follows:  $\ell_i$  and  $\ell_f$  denote the maximum level of refinement reached at the initial and final redshifts  $z_i$  and  $z_f$  while  $\Delta x$  gives the linear size of the highest-resolution elements found at  $z_f$  in proper units.

### 3 NUMERICAL SIMULATIONS

#### 3.1 Simulation setup

We ran several cosmological simulations of the formation of a massive ( $\sim 10^{12} M_\odot$ ) galaxy up to redshift  $z_f = 2$  using the fully Eulerian code RAMSES (Teyssier 2002). Each simulation started from the same initial conditions but employed different models for H<sub>2</sub> and SF, as detailed below (see Table 2 for a compact summary of our runs).

##### 3.1.1 Cosmological model

Each run adopted a flat  $\Lambda$ CDM cosmological model consistent with the *WMAP* 7-year data release (Komatsu et al. 2011). The corresponding parameters are:  $\Omega_m = 0.2726$ ,  $\Omega_b = 0.0456$ ,  $\sigma_8 = 0.809$ ,  $n_s = 0.963$  and  $h = 0.704$ . Here  $\Omega_m$  and  $\Omega_b$  denote the current density parameters for the total matter and the baryonic component, respectively;  $\sigma_8$  is the rms mass fluctuation in  $8 h^{-1}$  Mpc spheres, linearly extrapolated to  $z = 0$ ;  $n_s$  is the spectral index of the primordial density fluctuation spectrum, and  $h$  is the Hubble parameter expressed in units of  $100 \text{ km s}^{-1} \text{ Mpc}^{-1}$ .

##### 3.1.2 Initial conditions

Initial conditions for our simulations were generated with the MUSIC code (Hahn & Abel 2011) in the following way. We first ran a collisionless ‘parent’ simulation of a 71 Mpc box from  $z_i = 99$  to  $z_f = 0$  with a spatial resolution of 280 kpc. From the  $z = 2$  output, we randomly selected a DM halo with an approximate virial mass<sup>2</sup>  $M_{200} \sim 10^{12} M_\odot$  that also had a quiescent late-time accretion history. All particles within  $3 \times r_{200}$  (at  $z = 0$ , when the halo has a mass  $M_{200} \simeq 4 \times 10^{12} M_\odot$ ) were then traced back to the unperturbed linear density field and the comoving volume enclosing these particles ( $\sim (10 \text{ Mpc})^3$ ) was resampled at higher resolution in both DM and gas. The global setup includes

<sup>2</sup> We define the halo virial mass,  $M_{200}$ , as that within a sphere of radius  $r_{200}$  that encloses a mean density equal to 200 times the critical density for closure,  $\rho_c = 3H_0^2/8\pi G_N$  (where  $G_N$  is the gravitational constant).

several nested levels of refinement and periodic boundary conditions.

For our suite of simulations, Lagrangian volume elements within the high-resolution region have a length-scale of  $\sim 34.6$  comoving kpc. This is equivalent to resampling the entire initial 71 Mpc simulation volume with  $2048^3$  cells ( $2^{3\ell_i}$  with  $\ell_i = 11$ ). For our cosmological parameters and box size, the DM particle mass in these runs is  $m_{\text{DM}} = 1.3 \times 10^6 M_\odot$ .

##### 3.1.3 Numerical evolution

Each simulation was run using a version of the RAMSES code that was modified to include the various treatments of H<sub>2</sub> physics described in Section 2, as well as a new SF routine. RAMSES is an Adaptive Mesh Refinement (AMR) code which uses a second-order Godunov scheme to solve the hydrodynamic equations, while trajectories of stellar and DM particles are computed using a multi-grid Particle-Mesh solver. Between redshifts  $z = 9$  and 2, we output 140 simulation snapshots, equally spaced in 20 Myr intervals.

The AMR technique superimposes finer sub-grids on to the multilevel mesh used to generate the initial conditions, resulting in finer resolution in high-density regions. We employ a refinement strategy based on the standard ‘quasi-Lagrangian’ criterion: a cell is split if it contains more than eight DM particles or a baryonic mass greater than  $8 m_{\text{DM}} \Omega_b / (\Omega_m - \Omega_b)$ . To prevent catastrophic refinement, we enforce a constant physical resolution and match the maximum AMR-level to that attained in a pure DM-run, as discussed in section A8 of Scannapieco et al. (2012). This results in six additional levels of refinement before  $z_f$ , corresponding to a maximum level of  $\ell_f = 17$ , and to a spatial resolution of 180 pc at  $z = 2$ .

For the gas component, we assume an equation of state with polytropic index  $\gamma = 5/3$  and, to avoid spurious fragmentation, add thermal pressure using:  $\langle T \rangle = T_J (\langle n_{\text{H}} \rangle / n_J)^{\gamma-1}$ . Requiring the Jeans length to be resolved with at least four resolution elements (Truelove et al. 1997) one finds  $T_J \simeq 2500 (\Delta x / 180 \text{ pc})^{2/3} \text{ K}$  and  $n_J \simeq 3.8 (\Delta x / 180 \text{ pc})^{-4/3} \text{ cm}^{-3}$  for the Jeans temperature and density, where  $\Delta x$  is the (physical) length of the resolution element (Teyssier et al. 2010).

Our runs include SF, supernova (SNa) feedback and associated metal enrichment, as well as cooling from H, He

and metals. We adopt the uniform cosmic UV background of Haardt & Madau (2012) and approximate self-shielding of dense gas by exponentially suppressing it in cells where the gas density exceeds  $\langle n_H \rangle \sim 0.014 \text{ cm}^{-3}$  (Tajiri & Umemura 1998). In addition, we approximately account for interstellar LW radiation in order to solve for the abundance of molecular hydrogen (see Appendix A, for further details).

### 3.2 Star Formation

Cosmological simulations of galaxy formation lack the spatial resolution required to model the cold ISM. SF is therefore implemented stochastically by converting gas mass elements into star particles provided that certain physical conditions are satisfied. The prevailing approach is to relate the SFR density,  $\dot{\rho}_{\text{SF}}$ , to the total local gas density in a cell,  $\langle \rho_{\text{gas}} \rangle$  and a suitable time-scale,  $t_*$ , over which SF is expected to take place (Schmidt 1959). One common prescription is given by

$$\dot{\rho}_{\text{SF}} = \varepsilon \frac{\langle \rho_{\text{gas}} \rangle}{t_*}, \quad (15)$$

where  $t_*$  is the free-fall time of the gas,  $t_{\text{ff}} = \sqrt{3\pi/(32G_N \langle \rho_{\text{gas}} \rangle)}$  and  $\varepsilon$  is an efficiency parameter.

Our ‘standard’ run (STD) adopts this SF law only for convergent flows, within cells above a critical density,  $\langle n_* \rangle$ , and below a temperature threshold,  $T_c$ . We set  $T_c = 10^4$  K, and tune  $\varepsilon$  and  $\langle n_* \rangle$  in order to match the observed KS relation. This gives  $\langle n_* \rangle = 2/3 n_J$  and  $\varepsilon = 0.05$  which corresponds to a SF density threshold of  $\langle n_* \rangle \simeq 2.5 \text{ cm}^{-3}$ .

Alternatively, SF can be linked directly to the local density of molecular hydrogen (Pelupessy et al. 2006; Robertson & Kravtsov 2008; Gnedin et al. 2009; Gnedin & Kravtsov 2010; Feldmann et al. 2012; Zemp et al. 2012; Christensen et al. 2012; Kuhlen et al. 2012, 2013; Munshi et al. 2013; Jaacks et al. 2013; Munshi et al. 2014; Thompson et al. 2014):

$$\dot{\rho}_{\text{SF}} = \varepsilon \frac{\langle \rho_{H_2} \rangle}{t_*}. \quad (16)$$

Note that this does not require a density threshold, which arises naturally in the equations regulating the abundance of  $H_2$  (see Figure 1): low-density regions, where  $H_2$  formation is inefficient, are ineligible to form stars. Assuming that SF takes place exclusively within GMCs, whose typical densities are of the order of  $100 \text{ cm}^{-3}$ , we set  $t_*$  in equation (16) to be the minimum of the free-fall time-scales computed at the cell density and at  $100 \text{ cm}^{-3}$  (see also, Gnedin et al. 2009), and adopt  $\varepsilon = 0.05$ , as assumed for the STD run. Finally, in the DYN model, we only allow SF in convergent flows if the temperature of a cell is below  $10^4$  K.

### 3.3 Feedback, metal enrichment and molecules

Massive stars end their lives as Type II supernovae (SNe) which inject metals and energy into the ISM. Our runs adopt a stellar metallicity yield and an SNa return fraction consistent with a Kroupa (2001) initial mass function. We assume that each massive star releases  $10^{50} \text{ erg M}_{\odot}^{-1}$  of thermal energy into the ISM 10 Myr after their creation. To approximate the adiabatic expansion that follows a SNa explosion,

we turn off gas cooling for the next 40 Myr in the affected cells (e.g. Stinson et al. 2006; Agertz et al. 2013).

The impact of SNe on the distribution of  $H_2$  on  $\sim 100$  pc scales is far from certain, and current simulations of the ISM reach conflicting results (Krumholz 2014, and references therein). Some authors find that  $H_2$  is almost completely destroyed (Walch, personal communication) while others find that it quickly reforms due to the short cooling times of the densest regions (Rogers & Pittard 2013). We have bracketed this uncertainty by considering two extreme cases in our DYN model. In one, we leave the  $H_2$  distribution computed according to our non-equilibrium model unchanged in cells that have experienced recent SNa events. In a second simulation we set the  $H_2$  fraction to zero in cells that are directly influenced by SNe (i.e. those where the cooling is switched off) and we will refer to this run as DYN-SNe. No  $H_2$  destruction due to SNe has been considered in the simulations based on the KMT models; in this case,  $H_2$  is continuously ‘painted’ on the gas with no memory of the past conditions.

Finally, note that all our models for the formation of molecular hydrogen require the presence of dust (and hence metals) in order to catalyse the initial reactions. In fact, we do not follow  $H_2$  formation in the gas phase which is important only in very small objects (unresolved in our simulations) at early cosmic epochs (Abel et al. 1997, 1998). We therefore begin our simulations from pristine gas assuming an SF law given by equation (15). These runs are stopped at  $z = 9$ , at which point we introduce a metallicity floor of  $Z_{\text{floor}} = 10^{-3} Z_{\odot}$  in the regions that are uncontaminated by prior SF. The  $z = 9$  outputs are then used as the initial conditions for the runs that follow the distribution of  $H_2$  molecules from  $z = 9$  to  $z = 2$ . This procedure ensures that high-density, star-forming clumps are enriched with metals more efficiently at early times, and also approximately accounts for the enrichment expected from unresolved Population III SF (see, e.g., Wolfe et al. 2005; Wise et al. 2012, for more detail).

### 3.4 Identification of galaxies and haloes

In all simulation outputs, we identify gravitationally bound objects using the Amiga halo finder (AHF, Gill et al. 2004; Knollmann & Knebe 2009). Among other quantities, AHF returns the centre of each halo, its virial mass,  $M_{200}$ , and corresponding virial radius,  $r_{200}$ . (Note that halo masses and radii are computed using all matter.) Within each halo, we define the stellar and gas mass of the central galaxy as that enclosed within a radius  $r_{\text{gal}} = 0.1 r_{200}$  (e.g. Scannapieco et al. 2012), which gives  $r_{\text{gal}} \simeq 12.6$  (physical) kpc for the largest galaxy in the high-resolution region of our simulations at  $z = 2$ .

In order to link haloes between two consecutive outputs  $z_i < z_{i-1}$ , we consider a ‘descendant’ halo identified at  $z_i$ , and search for all of its ‘progenitor’ haloes at  $z_{i-1}$ . Progenitors are defined as haloes that have DM particles in common with the descendant, and the halo that provides most of the mass is referred to as the ‘main progenitor’. The history of the main galaxy is tracked by studying the evolution of the material within 10 per cent of the virial radius of the main progenitor, which we compute in each simulation output.

Model	$M_*$ ( $10^{11} M_\odot$ )	$M_{\text{gas}}^{\text{cold}}$ ( $10^{11} M_\odot$ )	$M_{\text{gas}}^{\text{hot}}$ ( $10^{11} M_\odot$ )	$M_{\text{H}_2}$ ( $10^{11} M_\odot$ )	SFR ( $M_\odot \text{ yr}^{-1}$ )	$\langle Z \rangle_{\text{M}}$ ( $Z_\odot$ )	$\langle Z \rangle_*$ ( $Z_\odot$ )	$\langle n_{\text{H}} \rangle_{20}^{\text{SFR}}$ ( $\text{cm}^{-3}$ )	$\langle n_{\text{H}} \rangle_{50}^{\text{SFR}}$ ( $\text{cm}^{-3}$ )	$\langle n_{\text{H}} \rangle_{80}^{\text{SFR}}$ ( $\text{cm}^{-3}$ )
STD	1.15	0.35	0.27	0.36	59.6	0.92	0.72	10.2	29.7	83.7
DYN	0.77	0.31	0.53	0.44	42.6	0.72	0.49	19.9	71.3	178.3
DYN-SNe	0.58	0.44	0.56	0.39	40.8	0.58	0.41	18.2	68.3	224.9
KMT-UV	0.74	0.43	0.42	0.39	58.4	0.72	0.51	9.2	21.1	52.7
KMT-EQ	1.36	0.27	0.06	0.12	67.0	1.07	0.82	4.8	10.4	23.7

**Table 3.** Physical properties for the main galaxy (i.e. measured within  $r_{\text{gal}} = 0.1 r_{200}$ ) at  $z = 2$ . The columns indicate the stellar, the cold ( $T < 10^4$  K), the hot ( $T > 10^4$  K) and the molecular gas mass, the SFR, the mass-weighted gas and stellar metallicities, and 20th, 50th and 80th percentiles of the SFR-weighted gas density.

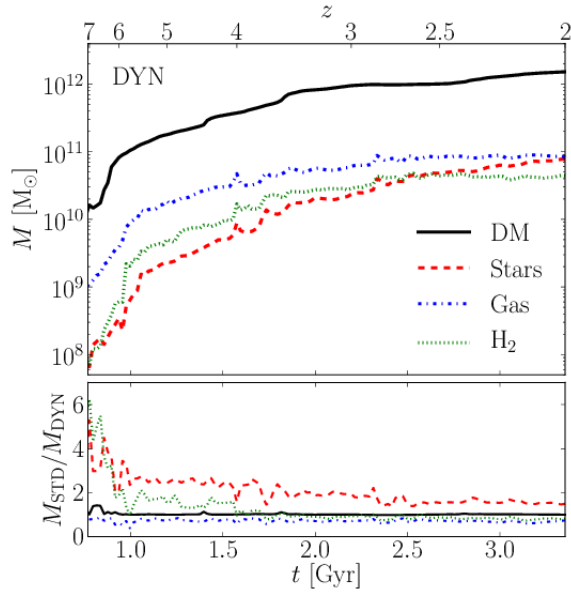


**Figure 3.** Assembly history of the main galaxy and its DM halo in the DYN run. The solid (black) line shows the evolution of the DM mass within  $r_{200}$ ; the mass of stars (red dashed lines), gas (blue dot-dashed lines) and molecular hydrogen (green dotted lines) measured within  $r_{\text{gal}}$  are also shown. The bottom panel shows the ratio between the mass (of each component) measured in the STD simulation to that in the DYN one.

## 4 RESULTS

### 4.1 Mass assembly history

In the top panel of Figure 3 we show the mass build-up of the main galaxy in different components for the DYN run over the redshift range  $z = 7-2$ . In the bottom panel, instead, we plot the same quantities for the STD run, but normalized to the masses in the DYN simulation. The mass-assembly history of the main halo (thick black line) is virtually identical for the two models: the halo has a final DM mass of  $1.8 \times 10^{12} M_\odot$  and exhibits a relatively quiescent recent formation history, with only three major-merging events that take place at  $z \sim 6$ ,  $\sim 4.4$  and  $\sim 3.5$ . At  $z = 2$  the halo contains more than 100 substructures with masses above  $10^8 M_\odot$  (corresponding to  $\sim 100$  DM particles), but more than 50 per cent of its stellar mass, and almost all of the molecular hydrogen, are located within the central galaxy.

The coloured lines show the time evolution of the masses of the different components within  $r_{\text{gal}}$ : stars are shown us-

ing a dashed (red) line, the total gas mass as a dot-dashed (blue) line, and the mass of molecular hydrogen as a dotted (green) line. Note that, in the STD run, the local  $\text{H}_2$  abundance is computed in post processing using the KMT-UV model.

We can distinguish three main evolutionary epochs, each lasting for approximately 1 Gyr: one in which the main galaxy is assembled out of several small sub-galactic objects (prior to  $z = 5.8$ ), followed by several minor mergers that take place between  $3.6 < z < 4$  and  $2.7 < z < 3.3$ , and a final quiescent approach to  $z = 2$  perturbed by the close passage of a relatively massive satellite at  $z \sim 2.15$ . Note that the stellar mass grows steadily with time while the gas and  $\text{H}_2$  masses remain approximately constant after  $z \sim 3$ .

The main galaxy in the STD model contains more stars than the DYN one at all epochs. Within the first Gyr, the STD galaxy forms five times more stars while the difference gradually decreases with time (the ratio reduces to  $\sim 1.5 - 2$  at  $t \simeq 3$  Gyr). Early SF is suppressed in the DYN run because  $\text{H}_2$  is created at a slow pace in a metal-poor environment. At  $z = 6$  ( $t = 0.9$  Gyr), the mean (mass-weighted) gas metallicity in the galaxy is  $\langle Z \rangle_{\text{M}} = 0.1 Z_\odot$  and the characteristic time-scale for  $\text{H}_2$  formation is as large as  $\tau_{\text{f}} = 1/(\mathcal{R}_{\text{f}} \langle n_{\text{H}} \rangle) \propto \langle Z \rangle^{-1} \sim 1$  Gyr (for the typical densities in the galaxy). In the following 3 Gyr, however, the ISM is steadily polluted with metals and  $\langle Z \rangle_{\text{M}}$  increases by roughly one order of magnitude. This promotes  $\text{H}_2$  formation at lower gas densities, and subsequently enhances SF. The simulations that are not shown in Figure 3 follow similar patterns to either the DYN or the STD models. For instance, in the KMT-UV and DYN-SNe simulations SF is also hindered at early times (in particular the DYN-SNe run forms nearly 20 per cent less stars than the DYN one at all times as the overall molecular mass is influenced by SNa explosions). On the other hand, the KMT-EQ run, where the  $\text{H}_2$  abundance is not directly influenced by the presence of a dissociating radiation field, does not show any significant difference with respect to the STD case.

To facilitate a comparison between the different models, we list in Table 3 some key properties of the main galaxies in each simulation at  $z = 2$ , including their total stellar mass,  $M_*$ , as well as the gas masses in hot, cold and molecular components. We also list the SFR (averaged over the past 20 Myr), the average gas and stellar metallicities and the 20th, 50th and 80th percentiles of the SFR-weighted gas density ( $\langle n_{\text{H}} \rangle^{\text{SFR}}$ ). (All quantities have been measured within  $r_{\text{gal}}$ .)

Due to their high spatial resolution, all our simulations form stars only at substantially higher gas densities than



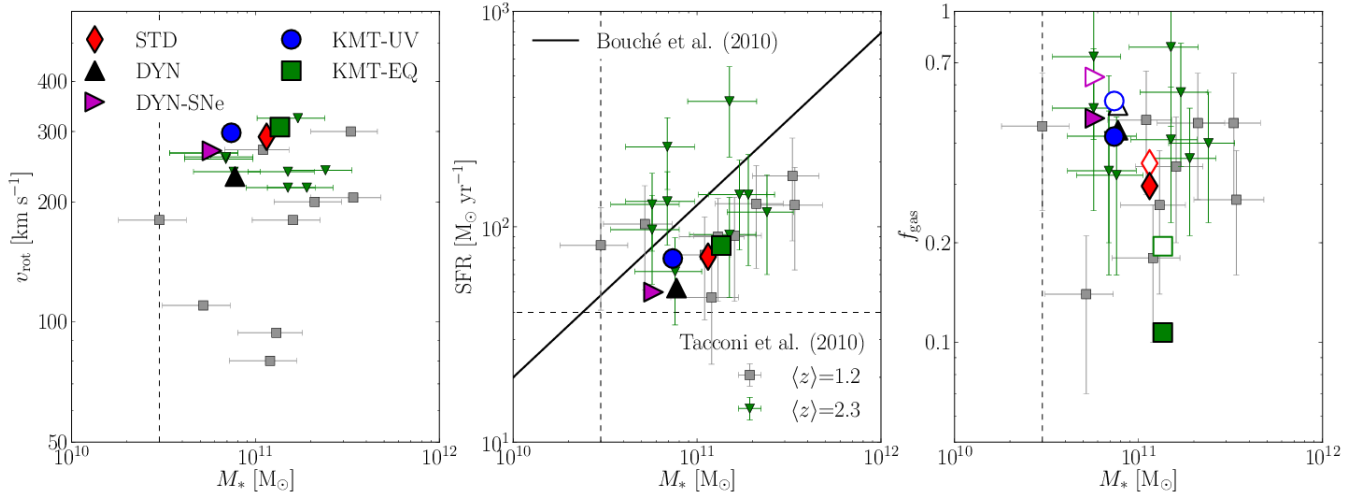


**Figure 4.** Gas rotational velocity (left-hand panel), star formation rate (middle panel) and gas fraction (right-hand panel) plotted versus the stellar mass of the main galaxy at  $z = 2$  for all runs. Heavy symbols correspond to our simulated galaxies, while small ones show the observed sample of Tacconi et al. (2010), which have been divided into low (grey squares) and high (green triangles) redshift subsamples. The solid black line in the middle panel is the galaxy SFR-main sequence at  $z = 2$  from Bouché et al. (2010). In the right-most panel, open symbols correspond to  $f_{\text{gas}}$  measured using the total gas mass, rather than the molecular component alone. The vertical and horizontal dashed lines show the selection criteria in stellar mass ( $M_* > 3 \times 10^{10} M_\odot$ ) and star formation rate ( $\text{SFR} > 40 M_\odot \text{ yr}^{-1}$ ) for the observational samples of Tacconi et al. (2010).

in most previous work. The SF threshold we adopt in the STD model is comparable to that used in the ERIS simulation (Guedes et al. 2011) and is several orders of magnitude above the commonly adopted value of  $\sim 0.01 - 0.1 \text{ cm}^{-3}$ . Our DYN and DYN-SNe models form stars at even higher densities (by more than a factor of 2, see Table 3). On the other hand, in the KMT-EQ and KMT-UV runs, stellar particles tend to be created in cells with somewhat lower densities than in the STD run. This has important consequences. In fact, when stars form only in correspondence of the highest density peaks, energy injection from SNe is strongly clustered and creates a very inhomogeneous ISM. Moreover, stellar feedback becomes more efficacious and plays a decisive role in shaping the structure of the emerging galaxy. For instance, highly peaked SF is more efficient in removing low-angular momentum gas at high redshift and thus reduces the mass of the final central bulge component (e.g. Robertson & Kravtsov 2008; Ceverino & Klypin 2009; Brook et al. 2011, 2012; Guedes et al. 2011).

In addition, in all runs in which SF is regulated by molecules (with the exception of KMT-EQ) the galaxy has a lower stellar mass and harbours a large gas reservoir. This is a direct consequence of suppression of SF at early times. For instance, in the DYN simulation, the gas reservoir is nearly 40 per cent higher than in the STD case.

## 4.2 Comparison with observations

### 4.2.1 Global properties of the galaxy at $z = 2$

In Figure 4 we compare several characteristics of our simulated galaxies at  $z = 2$  to observations of star forming galaxies at high-redshift. Outsized points in the left-hand panel plot the rotational velocity of the gas,  $v_{\text{rot}}$ , versus stellar mass for our simulations. Smaller symbols show the data set of Tacconi et al. (2010), which is divided into a

high ( $\langle z \rangle = 2.3$ ) and a low redshift sample ( $\langle z \rangle = 1.2$ ). To make a meaningful comparison with this data – for which  $v_{\text{rot}}$  was determined from CO line emission – we compute the rotational velocity using only the cold gas component.

The SFR versus stellar mass is shown in the middle panel. Large and small symbols have the same meaning as before. All our model galaxies, independent of the assumed  $H_2$  and SF laws, are forming stars at a similar rate, which is in good agreement with the observational data set, as well as with the theoretically determined SF main sequence at  $z = 2$  given in Bouché et al. (2010).

Finally, the right-hand panel shows the gas fraction, defined  $f_{\text{gas}} = M_{\text{gas}} / (M_{\text{gas}} + M_*)$ , versus galaxy stellar mass. Observationally,  $M_{\text{gas}}$  is determined from CO luminosity which is first converted into a molecular mass and then multiplied by a factor of 1.36 to account for helium atoms that should be well-mixed with the molecules. This estimate coincides with the actual gas mass only if the contribution from atomic hydrogen is negligible. In our simulations, this never holds true. Taking the DYN run at  $z = 2$  as an example, Table 3 shows that the cold atomic gas (H and He), the hot gas and the molecular hydrogen have all nearly identical masses. Therefore, in order to fairly compare the numerical results against the sample of Tacconi et al. (2010), we determine  $f_{\text{gas}}$  using the relationship  $M_{\text{gas}} = 1.36 M_{H_2}$ . These are shown as solid points in Figure 4. For comparison, we also show, using open symbols, the *total* gas fraction, which includes both atomic and molecular components.

In general, the rotational velocities, SFRs and gas fraction of our simulated galaxies agree well with the observational data set. Likewise, the simulations nicely match measurements of  $f_{\text{gas}}$  with the possible exception of the KMT-EQ model whose predictions (when based on  $H_2$  alone) fall below the observed data.

Another challenging test for the simulated galaxies is

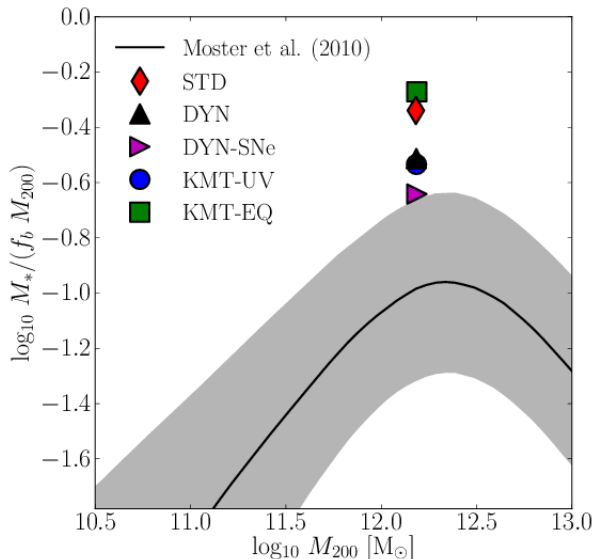


**Figure 5.** Stellar-to-halo-mass relation at  $z = 2$  for our simulations (solid symbols) and the observed relation at  $z = 2$  from (Moster et al. 2013, solid line). The grey shades indicate the  $1\sigma$  confidence level.

to check how their stellar mass-halo mass (SMHM) relation compares with the recent semi-empirical constraints which have been derived contrasting the galaxy number counts and the number density of DM haloes in  $N$ -body simulations with the abundance matching technique (see Behroozi et al. 2010, and references therein). In Figure 5 we plot the SMHM relation at  $z = 2$  (note that the stellar mass of the central galaxy is normalized to  $f_b M_{200}$ , where  $f_b = \Omega_b/\Omega_m$ ) for our simulations (solid symbols) and compare it with the recent observational results at  $z = 2$  by (Moster et al. 2013, shaded area and solid line). The STD and KMT-EQ runs are in tension with the data: they produce far too many stars given the mass of the DM halo. This is a well-known problem in cosmological simulations in which no strong feedback mechanisms beyond SNa explosions are included (see Scannapieco et al. 2012). However, the simulations in which the  $H_2$  abundance is computed with an explicit treatment of photo-dissociation behave differently. In fact, molecule-regulated SF acts as an effective feedback mechanism and helps reducing the stellar mass of the central galaxy. In particular, our DYN-SNe run lies within the  $1\text{-}\sigma$  uncertainty of the observed SMHM relation. Similar results are found at higher redshifts.

#### 4.2.2 The KS relation

In this section, we compare how the area-averaged SFR,  $\Sigma_{\text{SFR}}$  and corresponding gas surface densities,  $\Sigma_{\text{gas}}$  and  $\Sigma_{H_2}$ , relate to each other in our simulations. To do this, we compute all surface densities using a projection of the galaxies over a cylinder, with radius and height equal to  $r_{\text{gal}}$ , oriented along the  $z$ -axis of the computational box. In order to match observations that measure nebular emission lines ( $H\alpha$ , OII), which are sensitive to the light of young stars, we average the instantaneous SFR over the typical lifetime of OB stars, which we take to be 20 Myr. Note that we have verified

that our results are robust with respect to small changes in the orientation, radius and height of the cylinder as well as stellar age.

In the left-hand panel of Figure 6 we plot the KS relation for the total gas, while the right-hand panel shows the relation for the molecular gas. Outsized coloured symbols show the results for the main galaxy at different redshifts, while small grey squares refer to observations of individual galaxies (Daddi et al. 2010; Genzel et al. 2010). In each panel, power-law fits to observations of quiescent and starburst galaxies are shown with a dashed and dotted line, respectively.

By construction, the STD simulation perfectly reproduces the KS relation (expressed in terms of  $\Sigma_{\text{gas}}$ ) for normal galaxies as the parameters of the Schmidt law in equation (15) were tailored to achieve this result. The very same value of the efficiency parameter ( $\epsilon = 0.05$ ) has been used in all the other simulations together with equation (16). We find that all the runs are in good agreement (within the measured scatter) with the observed KS relation for the total as well as for the molecular gas.

#### 4.2.3 The $H_2/HI$ transition

Observational studies of the ISM show that the interface between the HI and  $H_2$ -dominated regions is rather sharp and occurs around a given hydrogen column density whose value depends on the local metallicity and on the intensity of UV radiation. Measurements from absorption spectra of distant quasars and nearby stars in the MW (Savage et al. 1977; Shull et al. 2004; Gillmon et al. 2006; Wolfire et al. 2008), the Large Magellanic Cloud (LMC Tumlinson et al. 2002) and the Small Magellanic Cloud (SMC Leroy et al. 2007) are reported in Figure 7 (coloured symbols). Here, we also plot data extracted from the DYN simulation (dots). To be consistent with the observational studies, we compute the  $H_2$  and HI column densities ( $N_{H_2}$  and  $N_{HI}$ ) and the average  $H_2$  fraction,  $f_{H_2} = 2N_{H_2}/N_{HI}$ , within a position-position-velocity data cube of  $180 \text{ pc} \times 180 \text{ pc} \times 40 \text{ km s}^{-1}$ . In order to make a meaningful comparison, we separate data with different metallicity ( $\bar{Z}$ ) and interstellar UV field ( $\bar{G}$ ). In the left-hand panel, we show the results extracted from the simulation at  $z \sim 2$  that match the physical conditions of the MW (i.e.  $\bar{Z} = Z_{\odot}$  and  $\bar{G} = 1$ , within a scatter of 30 per cent). In addition, we also plot recent measurements from a sample of 30 nearby galaxies with nearly solar metallicity from the HERACLES survey (Schruba et al. 2011). (Their column densities have been computed in tilted rings 15 arcsec wide and corrected for inclination.)

The middle and right-hand panels, instead, refer to the LMC ( $z \sim 3.5$  with  $\bar{Z} = 0.3 Z_{\odot}$  and  $\bar{G} = 10$ ) and the SMC ( $z \sim 5.5$  with  $\bar{Z} = 0.1 Z_{\odot}$  and  $\bar{G} = 100$ ), respectively. In all cases, we find that the DYN model is in excellent agreement with observations. The simulations that are not shown in Figure 7 give similar results. In particular, while the HI to  $H_2$  transition is virtually identical in the DYN-SNe and DYN runs, the simulations based on the KMT models correctly locate the value of  $N_{HI}$  at which  $f_{H_2} \sim 0.1$  but tend to predict too sharp a transition especially at  $z \sim 2$  when the gas metallicity is high.

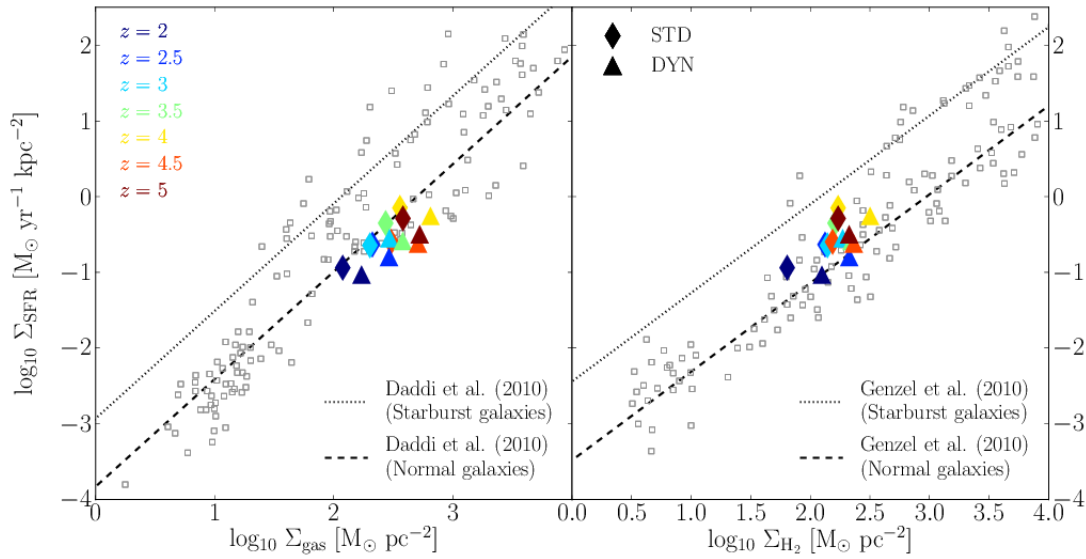


**Figure 6.** The KS relation for the total gas (left-hand panel) and for the molecular hydrogen (right-hand panel). Outsized coloured symbols show the relation measured for our main galaxy at different redshifts in the STD (diamonds) and DYN (triangles) simulations. We have integrated the gas and young stellar (i.e.  $t_s \leq 20$  Myr) mass distribution over a cylinder of radius and height  $r_{\text{gal}}$ , oriented along the  $z$ -axis of the computational box. The dashed and dotted lines show the average observed relations for normal/quiescent galaxies and merging/starbursts systems, respectively, and grey squares the observed data for individual galaxies from Daddi et al. (2010) and Genzel et al. (2010).

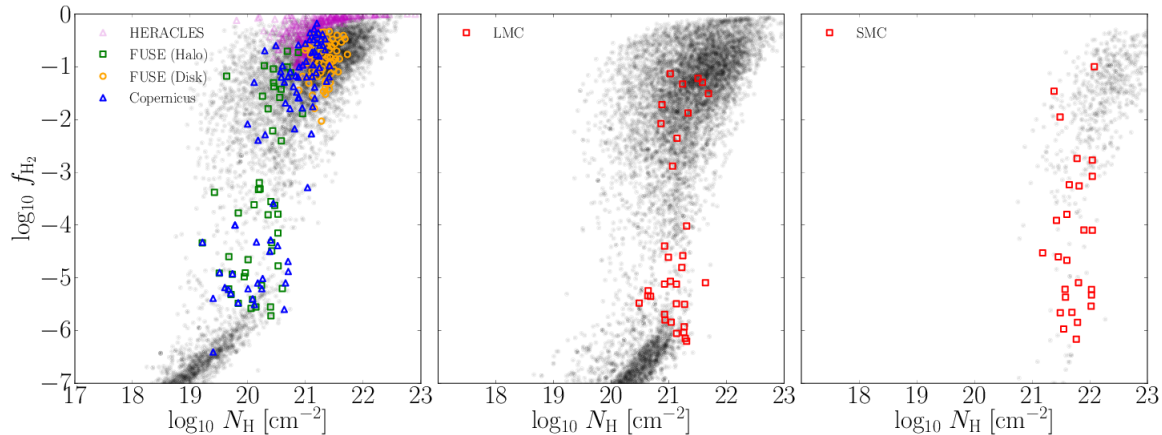


**Figure 7.** Total hydrogen column density,  $N_H = N_{\text{HI}} + 2N_{\text{H}_2}$ , versus the average  $H_2$  fraction,  $2N_{\text{H}_2}/N_H$ , measured in a position-velocity data cube of  $180 \text{ pc} \times 180 \text{ pc} \times 40 \text{ km s}^{-1}$  for the DYN simulation. Black points in the left-hand panel have been selected at  $z \sim 2$  and have, within a scatter of 30 per cent,  $\bar{Z} = Z_\odot$  and  $\bar{G} = 1$ . Coloured symbols show observations of the  $H_2/\text{HI}$  transition in the MW: blue triangles are taken from the Copernicus Survey (Savage et al. 1977), while orange circles and green squares from the FUSE disc (Shull et al. 2004) and halo survey (Gillmon et al. 2006), respectively. Purple points show observations from the HERACLES survey for a sample of 30 nearby galaxies (Schruba et al. 2011). Points in the middle panel are selected at  $z \sim 3.5$  and have mean metallicity and UV field (i.e.  $\bar{Z} = 0.3 Z_\odot$  and  $\bar{G} = 10$ ) comparable to the LMC (Tumlinson et al. 2002). Points in the right-hand panel have been selected at  $z \sim 5.5$  and have similar physical conditions (i.e.  $\bar{Z} = 0.1 Z_\odot$  and  $\bar{G} = 100$ ) to the SMC (Leroy et al. 2007).

### 4.3 The internal structure of the galaxies at $z = 2$

#### 4.3.1 The distribution of molecular hydrogen

Despite the fact that all models agree reasonably well with global observations of high-redshift galaxies, the detailed properties of the stellar, molecular and gaseous components in each simulation are rather different. For example, in Figure 8 we show the total hydrogen (left), the molecular hydrogen (centre) and the stellar particle (right) distributions at  $z = 2$  for the main galaxy in all of our simulations. The pan-

els show from top to bottom the results for the STD, DYN, DYN-SNe, KMT-UV and KMT-EQ runs, respectively.

The different assumptions used in these  $H_2$ -formation models are readily apparent in the  $H_2$  density distributions. Notice how including a sub-grid model for GMCs results in more molecular hydrogen in low-density gas. Nevertheless, the low densities in the outer regions contribute very little to the total  $H_2$ -mass budget in the DYN model.

A more quantitative analysis is provided in Figure 9, where we show the time evolution of the mean mass-

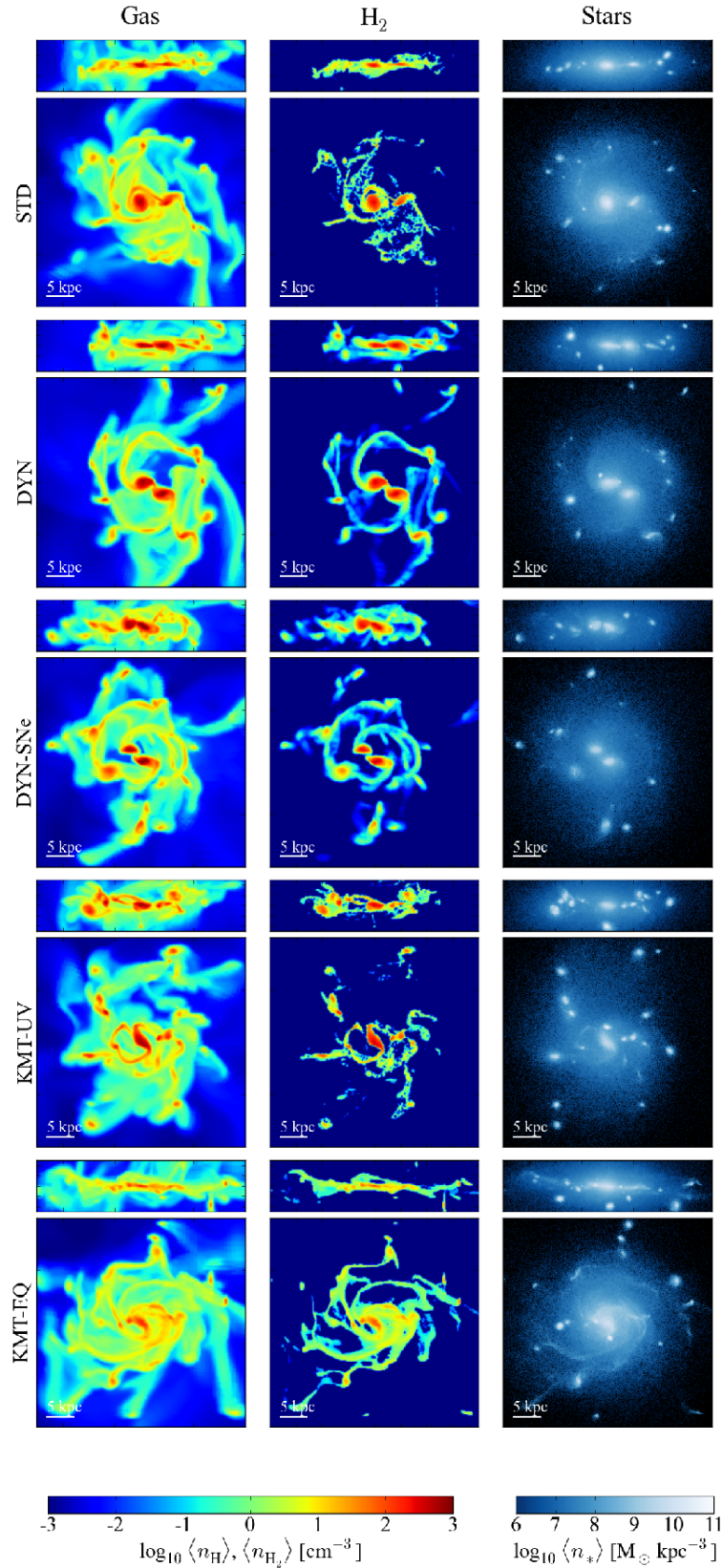


**Figure 8.** Face-on and edge-on views of the disc of the main galaxy for (from top to bottom) the STD, DYN, DYN-SNe KMT-UV and KMT-EQ runs at  $z = 2$  in a box of  $40 \times 40 \times 10$  kpc. From left to right, panels show the maximum hydrogen, H<sub>2</sub> and stellar densities along the line of sight, respectively.

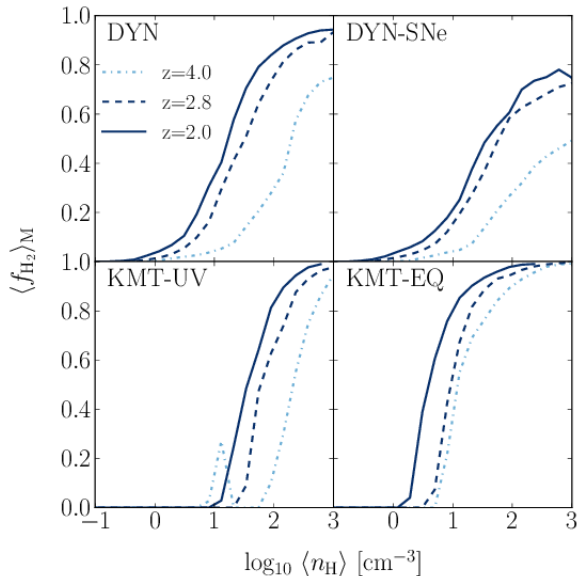


**Figure 9.** Distribution of the mass-weighted  $H_2$  fraction as a function of cell density for the models with molecule-regulated SF. Different line styles show results at three redshifts, as indicated in the legend.

weighted  $H_2$  fraction,  $\langle f_{H_2} \rangle_M$ , as a function of the cell density for all of our simulations. We focus on three different epochs: two merging events ( $z \sim 4$  and  $2.8$ ) and the final output at  $z = 2$ .

All models show a sharp  $H_2/HI$  transition which progresses towards lower densities with time. In the KMT models this is expected since atomic gas is converted into molecules only if its surface density is greater than a critical value that is inversely proportional to the local metallicity. Similarly, for the time-dependent models, higher metallicity gas produces  $H_2$  more rapidly. Therefore, the shift of the transition scale reflects the increasing metal content of the gas.

Finally, the DYN run shows two peculiarities: first, an appreciable  $H_2$  fraction is found at much lower mean densities than in the KMT models, and second,  $\langle f_{H_2} \rangle_M$  stays well below unity, even in the densest regions at early times. The first of these is due to the sub-grid density PDF adopted in the DYN model: the mean density of a cell is not representative of the regions in which  $H_2$  is formed. The latter is due to the effect of a time-dependent  $H_2$  formation model, which slowly gets to equilibrium as the metallicity of the galaxy increases with time. Note also that, when  $H_2$  destruction from SNa events is included, the DYN run predicts less molecular hydrogen in high-density regions. For instance, one can see in the top-right panel of Figure 9 that the DYN-SNe run shows  $\sim 20$  per cent less molecular hydrogen at  $\langle n_H \rangle > 10 \text{ cm}^{-3}$ .

A key assumption of the  $H_2$ -models that we have considered here is that the abundance of dust traces the gas metallicity. Since  $H_2$  forms rapidly in dust-rich environments, this hypothesis has important consequences. In fact, at all epochs and in all simulations, we measure a tight correlation between the mass in metals,  $M_Z$ , and the  $H_2$  mass,  $M_{H_2}$ , at the cell level. For example, in the DYN model, the relation between  $M_Z$  and  $M_{H_2}$  can be accurately described by a

Model	$M_*(r < 1 \text{ kpc})$ ( $10^{10} M_\odot$ )	$t_s(r < 1 \text{ kpc})$ (Gyr)
STD	1.1	1.1
DYN	0.4	0.6
DYN-SNe	0.3	0.5
KMT-UV	0.4	0.7
KMT-EQ	0.9	1.3

**Table 4.** Stellar mass and mean stellar age within 1 kpc from the galaxy at  $z = 2$  for all the runs.

power law; the linear correlation coefficient in the log – log plane is  $\sim 0.99$ , and similar values are found for the KMT models, above a threshold mass of metals,  $M_Z \gtrsim 2 \times 10^3 M_\odot$ . The best-fitting power-law parameters, however, evolve slowly with redshift. For example, in the DYN run, we find that  $M_{H_2} \propto M_Z^\alpha$  where  $\alpha$  grows smoothly from 0.96 to 1.07 in the redshift interval  $5 < z < 2$ . The constant of proportionality is  $\sim 30$  when masses are measured in units of  $M_\odot$ . After performing a careful calibration against the parameters of the sub-grid models, this tight correlation could be exploited to run computationally inexpensive simulations that link the abundance of molecular hydrogen directly to that of the metals.

#### 4.4 Build-up of the galaxy and its satellites

The evolution of the  $H_2$  (or total gas) profile in our simulations determines the structure of the stellar disc. In order to better assess the differences between our runs, we study the radial distribution of stars at  $z = 2$  within the galaxy in bins of stellar age. We choose the bins so that, in the STD run, the stellar mass produced in each is equal to one fifth of the galaxy’s total stellar mass at  $z = 2$  (corresponding to age bins of  $[3.35, 1.80]$ ,  $[1.80, 1.39]$ ,  $[1.39, 0.98]$ ,  $[0.98, 0.48]$ ,  $[0.48, 0]$  Gyr). The results for the STD (left-hand panels) and DYN (right-hand panels) runs are plotted in the top row of Figure 10 (qualitatively similar results are obtained when using the DYN-SNe model instead of DYN). One can see that the DYN model shows significant differences in the age distribution of stars, especially at early formation epochs (represented with darker shades of blue) and in the innermost 5 kpc. These regions are populated by younger stars in DYN than in the STD case. For instance, the mean age of the stellar particles located at  $r < 1 \text{ kpc}$  is 1.1 Gyr in the STD simulation, but only 0.6 Gyr in DYN. The total stellar mass within 1 kpc from the galaxy centre at  $z = 2$  is also different. In fact, we find values of  $M_*(r < 1 \text{ kpc}) = 1.1 \times 10^{10} M_\odot$  for the STD run and  $0.4 \times 10^{10} M_\odot$  for the DYN one. (For all the other models see Table 4.)

To explain the origin of this difference, we separate the stars that formed in the central galaxy of the most massive progenitor halo (second row in Figure 10) from those that formed in other haloes (third row). In the STD model, nearly 66 per cent of the stars in the first quintile of the age distribution ( $z > 4$ ) does not form in the most massive progenitor. On the other hand, in the DYN simulation, only 8 per cent of the final stellar mass is created at such early times mostly in the central galaxy of the most massive progenitor (41 per cent) and in other haloes (59 per cent). A visual impression can be formed from Figure 11 where we

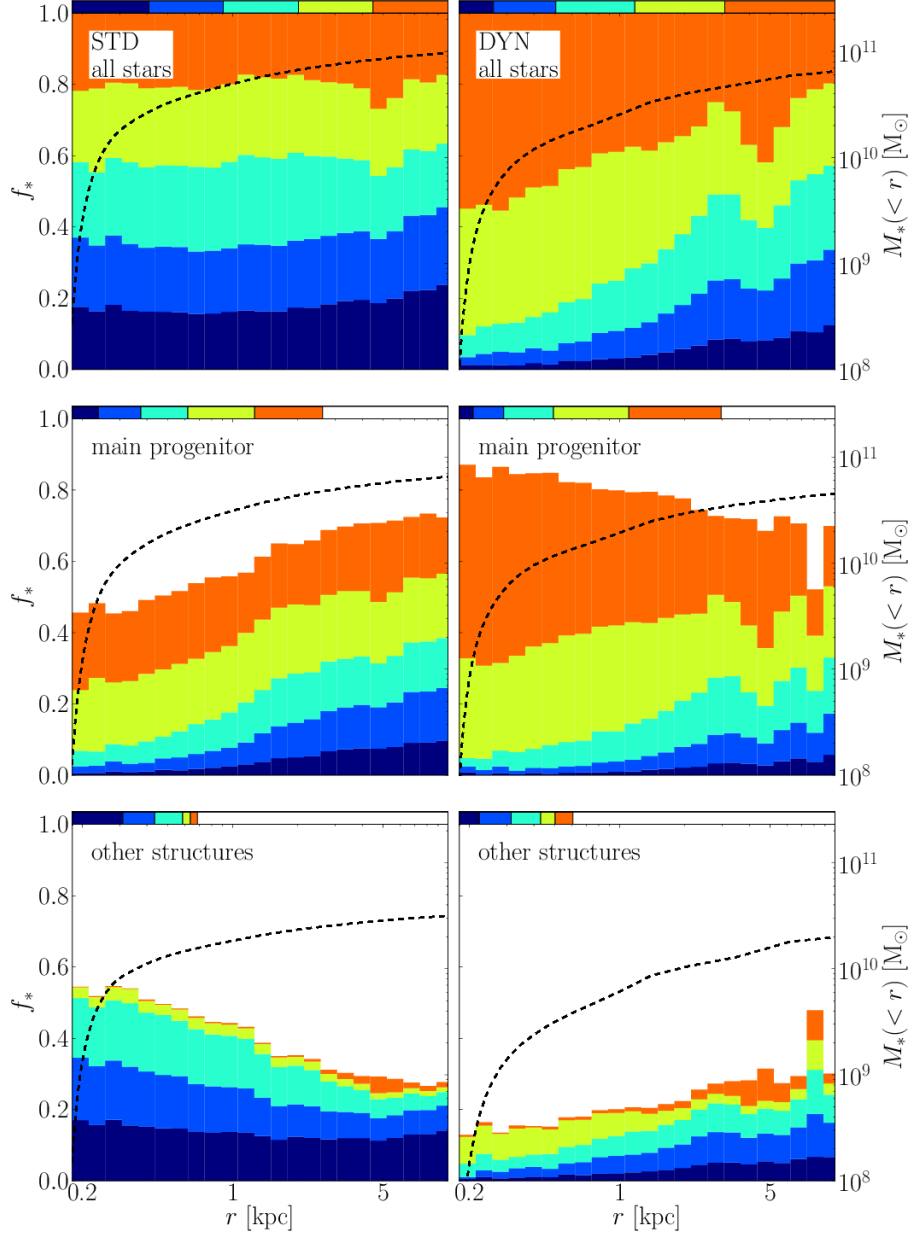


**Figure 10.** The radial distribution of stars within the galaxy at  $z = 2$  for the STD (left-hand panels) and DYN (right-hand panels) simulations. The first row shows the distribution for all the stars in the galaxy, the second one for the stars formed in the most massive progenitor of the host halo at  $z = 2$ , the third one for the stars formed in other structures. Different coloured regions indicate the fraction of stars as a function of radius sorted in five stellar age bins: [3.35, 1.80], [1.80, 1.39], [1.39, 0.98], [0.98, 0.48], [0.48, 0] Gyr (colour-coded so that dark-blue shades corresponds to earlier epochs). These bins are chosen so that, in the STD run, the stellar mass produced in each of them is equal to one fifth of the galaxy stellar mass at  $z = 2$ . The coloured bars on top of each panel are scaled in size to match the fraction of stellar mass that is formed within each time bin. The cumulative stellar mass distribution (dashed lines) is also plotted in each panel.

compare the spatial distribution of DM and stars extracted from the two simulations in the region surrounding the most massive progenitor at  $z = 5.5$ .

At this redshift, in the STD run, 99 per cent of the haloes with  $M > 10^9 M_\odot$  (i.e. above the mass threshold where SF is suppressed by the cosmic reionization of hydrogen) contain some stars while only 33 per cent do in the DYN simulation. This striking difference is due to the fact that most low-mass haloes (with  $M \lesssim 10^{10} M_\odot$ ) in the

DYN model cannot efficiently form molecular hydrogen at early times. In fact, their dust content and central densities are too low to promote efficient  $H_2$  formation, resulting in much lower SFRs. We find that their characteristic  $H_2$  formation time,  $\tau_f = 1/(\mathcal{R}_f \langle n_H \rangle)$ , is several orders of magnitude larger than the age of the Universe. Therefore, many low-mass haloes stay gas rich but dark (similar conclusions have been reached using the KMT-EQ model by

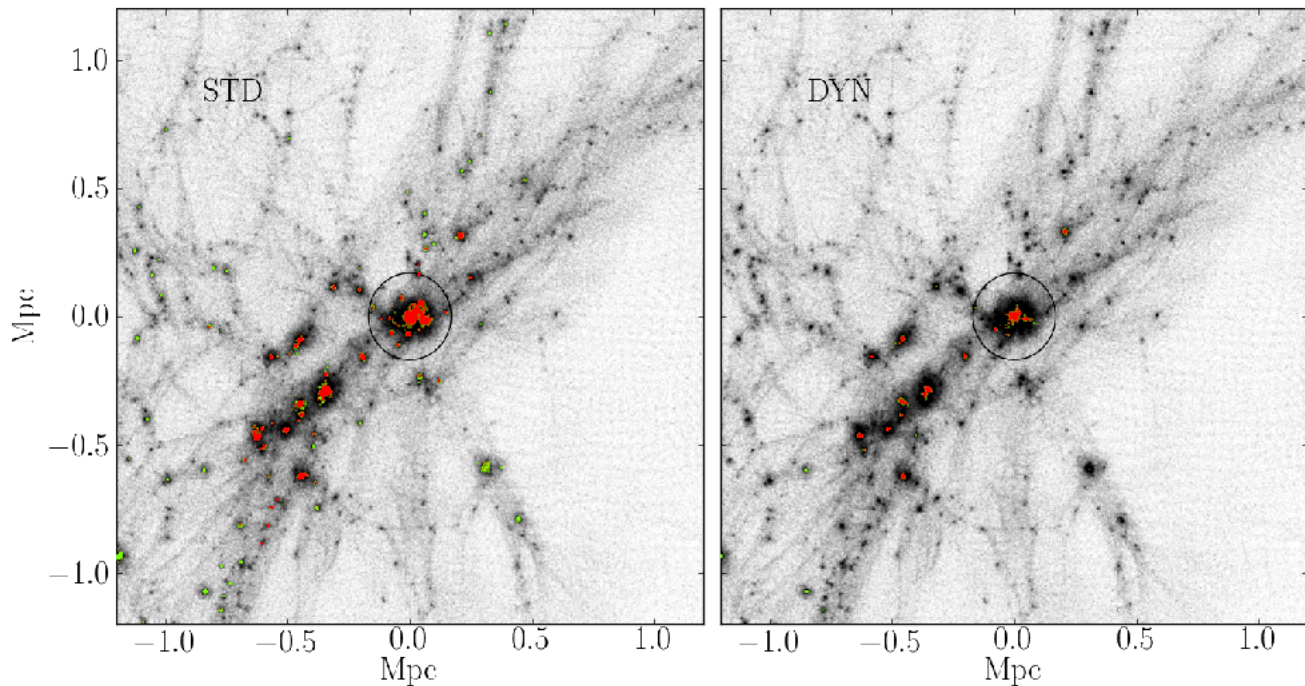


**Figure 11.** Comoving spatial distribution (in a 1.2 Mpc thick slice projected along one axis of the simulation box) of the DM (black points) and of the stars (green points) at  $z = 5.5$  for the STD (left-hand panel) and DYN (right-hand panel) runs. Stars that are found in the main galaxy at  $z = 2$  are shown in red. The plots are centred on the main halo, indicated with a black circle of radius  $r_{200}$ .

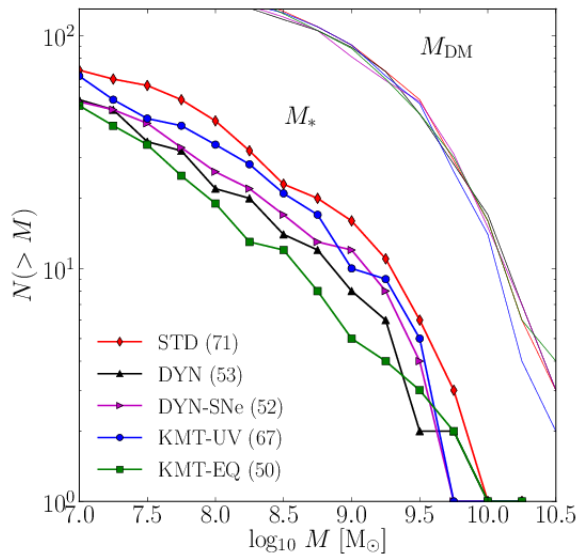


**Figure 12.** Cumulative distribution of the DM (thin lines) and stellar mass (connected points) of substructures within the virial radius of the most massive halo at  $z = 2$  for the STD (red), DYN (black), DYN-SNe (magenta), KMT-UV (blue) and KMT-EQ (green) runs. The total number of substructures (with  $r < r_{200}$  and hosting at least 100 stellar particles) is indicated in parenthesis.

Kuhlen et al. 2012, 2013; Jaacks et al. 2013; Thompson et al. 2014).

This phenomenon has strong implications for the assembly of the galaxy in our simulations. In the STD run, the main-progenitor galaxy is built up by a sequence of merg-

ers between objects with extended stellar components. On the other hand, in the DYN simulation, the same mergers provide gas-rich haloes with a few compact stellar distributions. Once a well defined central galaxy is in place, the merger history in the two models is nearly identical. However, the different rules with which SF and feedback take place produce a clumpier stellar pattern in the DYN model while the STD run more often develops grand design spiral arms in between major merging events. Off-centre mergers between substructures produce large clumps in both models (see Figure 8). In particular, a massive ( $M_{\text{tot}} = 4 \times 10^{10} M_{\odot}$ ) gas-rich condensation forms at  $z = 2.6$  in the DYN model and orbits within a few kpc from the galactic centre afterwards. A first encounter between this object and the central stellar clump of the main galaxy takes place at  $z = 2.4$ . This event heats the distribution of stellar orbits in the core of the DYN galaxy and scatters the old stars (that were previously concentrated in the middle) over a more extended area (see the bottom right panel in Figure 10). SF in the central regions of the galaxy is also boosted at this time (see the right-hand panel in the second row of Figure 10). In both models, the late history of the galaxy is characterized by a close encounter with a satellite at  $2.1 < z < 2.2$  which mildly distorts the gas and stellar distributions.

Finally, we focus our attention on the distribution of satellite galaxies at  $z = 2$ . Figure 12 shows, for all models, the cumulative number of substructures that are found within the virial radius of the main halo as a function of their DM and stellar masses. While the number of DM clumps is virtually identical in all runs, the STD model produces a larger number of bright satellites than any other run (approximately 30 per cent more than in the DYN simulation and 10 to 30 per cent more in the other models). This is a

direct consequence of the suppression of SF in metal-poor, low-mass haloes that we have already discussed above. We conclude that molecule-regulated SF can act as an effective feedback mechanism that may alleviate the satellite problem of the CDM scenario (e.g. Klypin et al. 1999; Moore et al. 1999). Further study will be necessary to determine whether this conclusion also applies to low redshift galaxies.

## 5 CONCLUSIONS

We have presented a sub-grid model for tracking the non-equilibrium abundance of molecular hydrogen in cosmological simulations of galaxy formation. The novelty of the model is that it phenomenologically accounts for the distribution of unresolved sub-grid densities determined from observations and simulations of the turbulent ISM. In this sense, it improves upon previous time-dependent schemes (e.g. Gnedin et al. 2009; Christensen et al. 2012) in which the  $\text{H}_2$  formation rate on dust grains is amplified by a fixed clumping factor.

We have implemented our model in the RAMSES code in order to run simulations that track the evolution of the  $\text{H}_2$  content of a massive galaxy at  $z = 2$ , and to study the imprint of  $\text{H}_2$ -regulated SF. The resulting  $\text{H}_2$  fractions in different environments spanning a vast range of gas metallicities and interstellar UV fields are consistent with observations of the Milky Way Galaxy, the LMC and the SMC.

In order to better understand what determines the properties of a galaxy, we ran a suite of simulations of the same DM halo, each with a different prescription for computing the  $\text{H}_2$  distribution. In the runs where  $\text{H}_2$  is calculated explicitly, SF was regulated by the local  $\text{H}_2$  abundance, while, for another (STD), we adopted the traditional Schmidt law based on the total gas density. Our main findings can be summarized as follows:

(i) All simulations produce a galaxy which is in broad agreement with several high-redshift observational data sets. However, the different models for star and  $\text{H}_2$  formation result in important differences in the stellar and gas masses of the galaxies (see Table 3).

(ii) In particular, if SF is molecule-regulated and the  $\text{H}_2$  abundances are computed with a detailed treatment of photo-dissociation including a simplified radiative-transfer scheme:

(a) The galaxy produces less stars and is in better agreement with the observed stellar-to-halo mass relation with respect to the STD model (which, however, cannot be ruled out as we did not study the effect of increasing the spatial resolution of the simulations).

(b) The galaxy harbours a larger gas reservoir and its gas fraction better matches observations of high redshift galaxies.

(c) Early SF is inhibited in metal-poor haloes with mass  $M \lesssim 10^{10} M_\odot$  in which gas and dust densities are too low to trigger efficient conversion of HI into  $\text{H}_2$ . As a result, the main galaxy assembles by accreting many gas-rich substructures and, consequently, hosts a younger stellar population and harbours a larger cold gas reservoir than in the STD case. Also, the number of satellites

of the main galaxy at  $z = 2$  is reduced by 30 per cent at all stellar masses compared with the STD simulation.

(iii) Regardless of the  $\text{H}_2$  model:

(a) The main galaxy in our simulations (with the exception of the KMT-EQ model) has similar spatial distribution and total mass of molecular hydrogen at  $z = 2$ . This is mainly due to the fact that the average metallicity of the gas in its dominant progenitors is already  $0.1 Z_\odot$  at  $z = 9$ . As a result,  $\text{H}_2$  formation is rapid, mitigating any subtle differences independent of whether stars form from atomic or molecular gas.

(b) The molecular mass in a cell scales linearly with that of the metals (above a model-dependent threshold density). This is a consequence of assuming that dust traces the metals in the simulations.

(iv) If  $\text{H}_2$  destruction by SNe is substantial, SF is suppressed by nearly 20 per cent at all times relative to an identical model in which this destruction channel is neglected.

(v) Contrary to the assumption that gas is fully molecular in high-redshift galaxies (commonly used to interpret CO observations, e.g. Genzel et al. (2010); Tacconi et al. (2010); Magnelli et al. (2013)), the atomic gas fraction in our simulated galaxy is comparable to the molecular contribution, independent of the  $\text{H}_2$  formation model.

(vi) Using the STD model to form stars, but ‘painting on’  $\text{H}_2$  in post-processing using the KMT-UV prescription, gives a reasonable estimate of the total  $\text{H}_2$  mass of the galaxy. However, as already mentioned above, the resulting galaxy contains more stars (in particular old stars) than in all of the molecule-regulated schemes.

Although our non-equilibrium  $\text{H}_2$  model represents a significant improvement over previous methods, many challenges remain. For instance, we have assumed that the sub-grid density PDF of GMCs can be accurately described by a lognormal distribution. This is based on several observations of molecular clouds which, in some cases, show high-density tails in star forming regions (e.g. Kainulainen et al. 2009; Schneider et al. 2013). Several complex physical phenomena like energy injection, turbulence, gravity and external compression influence the density structure of molecular clouds. Yet, numerical studies of the ISM have shown that the lognormal model is a good approximation when an isothermal gas flow is supersonically turbulent (e.g. Vazquez-Semadeni 1994; Glover & Mac Low 2007a,b; Federrath et al. 2009; Federrath & Klessen 2013). Power-law tails in the high-density regime form under the presence of self-gravity (which generates dense cores and super-critical filaments). Non-isothermal turbulence can also increase the occurrence of dense clumps. None the less, these uncertainties are likely sub-dominant to those associated with modelling the effects of SNa feedback on GMCs, which must be tackled with small-scale simulations of the ISM.

In addition, we have set the dispersion of the lognormal density distribution to be  $\sigma \simeq 1.5$ , consistent with a constant clumping factor  $C_\rho = 10$ . This choice was motivated by theoretical work that relates local density enhancements to the three-dimensional rms Mach number,  $\mathcal{M}$ , with values of  $\mathcal{M} \sim 5.5$  (e.g. Padoan et al. 1997; Ostriker et al. 2001; Price et al. 2011). Moreover, the same value for the clumping factor has been adopted in the literature to best match



the  $H_2$  content in observations and simulations (e.g. Gnedin et al. 2009; Christensen et al. 2012). However, observations of GMCs have revealed substantial variations in the Mach number (Schneider et al. 2013). In future implementations, the realism of our model can be improved by adjusting the clumping factor (as well as the PDF of the sub-grid density) in cells with different mean densities and temperatures. From the technical point of view, this is straightforward to do: the difficulty lies in linking the mean properties of a cell to the sub-grid parameters that regulate the density PDF. One intriguing possibility could be to implement a simplified description of supersonic turbulence along the lines of that proposed by Teyssier et al. (2013). We plan to return to these issues in future work.

## ACKNOWLEDGEMENTS

We wish to thank our referee for a constructive report that has improved this paper. We also thank Romain Teyssier and Tom Abel for helpful discussions and acknowledge support from Mark Labadens for the software PyMSES and from Oliver Hahn for the MUSIC code. We are also grateful to Andreas Schruba for kindly providing us with data from the HERACLES survey. This work was supported by the Deutsche Forschungsgemeinschaft (DFG) through the project SFB 956 *Conditions and Impact of Star Formation*, sub-project C4. MT was supported through a stipend from the International Max Planck Research School (IMPRS) for Astronomy and Astrophysics in Bonn. We acknowledge that the results of this research have been achieved using the PRACE-2IP project (FP7 RI-283493) resources HeCTOR based in the UK at the UK National Supercomputing Service and the Abel Computing Cluster based in Norway at the University of Oslo.

## REFERENCES

- Abel T., Anninos P., Norman M. L., Zhang Y., 1998, *ApJ*, 508, 518
- Abel T., Anninos P., Zhang Y., Norman M. L., 1997, *New Astron.*, 2, 181
- Agertz O., Kravtsov A. V., Leitner S. N., Gnedin N. Y., 2013, *ApJ*, 770, 25
- Behroozi, P. S., Conroy, C., & Wechsler, R. H. 2010, *ApJ*, 717, 379
- Bigiel F., Leroy A., Walter F., Brinks E., de Blok W. J. G., Madore B., Thornley M. D., 2008, *AJ*, 136, 2846
- Bouché N., et al. 2010, *ApJ*, 718, 1001
- Brook, C. B. et al. 2011, *MNRAS*, 415, 1051
- Brook, C. B., Stinson, G., Gibson, B. K., Wadsley, J., & Quinn, T. 2012, *MNRAS*, 424, 1275
- Burke J. R., Hollenbach D. J., 1983, *ApJ*, 265, 223
- Carilli C. L., Walter F., 2013, *ARA&A*, 51, 105
- Cazaux S., Spaans M., 2004, *ApJ*, 611, 40
- Cazaux S., Spaans M., 2009, *A&A*, 496, 365
- Ceverino, D., & Klypin, A. 2009, *ApJ*, 695, 292
- Christensen C., Quinn T., Governato F., Stilp A., Shen S., Wadsley J., 2012, *MNRAS*, 425, 3058
- Daddi E., et al., 2010, *ApJ*, 714, L118
- Dobbs C. L., et al., 2013, preprint (arXiv:1312.3223)
- Draine B. T., Bertoldi F., 1996, *ApJ*, 468, 269
- Federrath C., Klessen R. S., 2013, *ApJ*, 763, 51
- Federrath C., Klessen R. S., Schmidt W., 2009, *ApJ*, 692, 364
- Feldmann R., Gnedin N. Y., Kravtsov A. V., 2011, *ApJ*, 732, 115
- Feldmann, R., Gnedin, N. Y., & Kravtsov, A. V. 2012, *ApJ*, 758, 127
- Genzel R., et al., 2010, *MNRAS*, 407, 2091
- Gill S. P. D., Knebe A., Gibson B. K., 2004, *MNRAS*, 351, 399
- Gillmon K., Shull J. M., Tumlinson J., Danforth C., 2006, *ApJ*, 636, 891
- Glover S. C. O., Clark P. C., 2012, *MNRAS*, 426, 377
- Glover S. C. O., Mac Low M.-M., 2007a, *ApJS*, 169, 239
- Glover S. C. O., Mac Low M.-M., 2007b, *ApJ*, 659, 1317
- Gnedin N. Y., Kravtsov A. V., 2011, *ApJ*, 728, 88
- Gnedin N. Y., Tassis K., Kravtsov A. V., 2009, *ApJ*, 697, 55
- Gnedin, N. Y., & Kravtsov, A. V. 2010, *ApJ*, 714, 287
- Guedes, J., Callegari, S., Madau, P., & Mayer, L. 2011, *ApJ*, 742, 76
- Haardt F., Madau P., 2012, *ApJ*, 746, 125
- Hahn O., Abel T., 2011, *MNRAS*, 415, 2101
- Hopkins P. F., Kereš D., Murray N., Quataert E., Hernquist L., 2012, *MNRAS*, 427, 968
- Jaacks, J., Thompson, R., & Nagamine, K. 2013, *ApJ*, 766, 94
- Kainulainen J., Beuther H., Henning T., Plume R., 2009, *A&A*, 508, L35
- Kennicutt Jr. R. C., 1989, *ApJ*, 344, 685
- Kennicutt Jr. R. C., 1998, *ApJ*, 498, 541
- Kennicutt Jr. R. C., Calzetti D., Walter F., Helou G., Hollenbach D. J., Armus L., Bendo G., 2007, *ApJ*, 671, 333
- Knollmann S. R., Knebe A., 2009, *ApJS*, 182, 608
- Komatsu E., et al., 2011, *ApJS*, 192, 18
- Kroupa P., 2001, *MNRAS*, 322, 231
- Krumholz, M. R. 2014, preprint (arXiv:1402.0867)
- Krumholz M. R., Gnedin N. Y., 2011, *ApJ*, 729, 36
- Krumholz M. R., McKee C. F., Tumlinson J., 2008, *ApJ*, 689, 865
- Krumholz M. R., McKee C. F., Tumlinson J., 2009, *ApJ*, 693, 216
- Kuhlen M., Krumholz M. R., Madau P., Smith B. D., Wise J., 2012, *ApJ*, 749, 36
- Kuhlen, M., Madau, P., & Krumholz, M. R. 2013, *ApJ*, 776, 34
- Klypin, A., Kravtsov, A. V., Valenzuela, O., & Prada, F. 1999, *ApJ*, 522, 82
- Leitherer C., Schaerer D., Goldader J. D., González Delgado R. M., Robert C., Kune D. F., de Mello D. F., Devost D., Heckman T. M., 1999, *ApJS*, 123, 3
- Leroy A., Bolatto A., Stanimirovic S., Mizuno N., Israel F., Bot C., 2007, *ApJ*, 658, 1027
- Leroy A. K., Walter F., Brinks E., Bigiel F., de Blok W. J. G., Madore B., Thornley M. D., 2008, *AJ*, 136, 2782
- McKee C. F., Krumholz M. R., 2010, *ApJ*, 709, 308
- Magnelli, B., et al. 2013, *A&A*, 553, A132
- Micic M., Glover S. C. O., Federrath C., Klessen R. S., 2012, *MNRAS*, 421, 2531

- Moore, B., Ghigna, S., Governato, F., Lake, G., Quinn, T., Stadel, J., Tozzi, P., 1999, *ApJL*, 524, L19
- Moster, B. P., Naab, T., & White, S. D. M. 2013, *MNRAS*, 428, 3121
- Munshi, F., et al. 2013, *ApJ*, 766, 56
- Munshi, F., Christensen, C., Quinn, T. R., Governato, F., Wadsley, J., Loebman, S., Shen, S., 2014, *ApJ*, 781, L14
- Ostriker E. C., Stone J. M., Gammie C. F., 2001, *ApJ*, 546, 980
- Padoan P., Nordlund A., Jones B. J. T., 1997, *MNRAS*, 288, 145
- Pelupessy F. I., Papadopoulos P. P., van der Werf P., 2006, *ApJ*, 645, 1024
- Price D. J., Federrath C., Brunt C. M., 2011, *ApJL*, 727, L21
- Robertson, B. E., & Kravtsov, A. V. 2008, *ApJ*, 680, 1083
- Rogers H., Pittard J. M., 2013, *MNRAS*, 431, 1337
- Savage B. D., Bohlin R. C., Drake J. F., Budich W., 1977, *ApJ*, 216, 291
- Scannapieco C., et al., 2012, *MNRAS*, 423, 1726
- Schmidt M., 1959, *ApJ*, 129, 243
- Schneider N., André P., Könyves V., Bontemps S., Motte F., Federrath C., Ward-Thompson D., Arzoumanian D., 2013, *ApJL*, 766, L17
- Schruba, A. et al. 2011, *AJ*, 142, 37
- Shull, J. M., Anderson, K., Tumlinson, J., & FUSE Science Team 2004, *BAAS*, 36, 772
- Stinson G., Seth A., Katz N., Wadsley J., Governato F., Quinn T., 2006, *MNRAS*, 373, 1074
- Sternberg, A., Le Petit, F., Roueff, E., & Le Bourlot, J. 2014, *ApJ*, 790, 10
- Tacconi L. J., et al., 2010, *Nature*, 463, 781
- Tajiri Y., Umemura M., 1998, *ApJ*, 502, 59
- Teyssier R., 2002, *A&A*, 385, 337
- Teyssier R., Chapon D., Bournaud F., 2010, *ApJ*, 720, L149
- Teyssier R., Pontzen A., Dubois Y., Read J. I., 2013, *MNRAS*, 429, 3068
- Thompson, R., Nagamine, K., Jaacks, J., & Choi, J.-H. 2014, *ApJ*, 780, 145
- Tielens A. G. G. M., Hollenbach D., 1985, *ApJ*, 291, 722
- Truelove J. K., Klein R. I., McKee C. F., Holliman II J. H., Howell L. H., Greenough J. A., 1997, *ApJL*, 489, L179
- Tumlinson J., et al., 2002, *ApJ*, 566, 857
- Vazquez-Semadeni E., 1994, *ApJ*, 423, 681
- Wise J. H., Turk M. J., Norman M. L., Abel T., 2012, *ApJ*, 745, 50
- Wolfe A. M., Gawiser E., Prochaska J. X., 2005, *ARA&A*, 43, 861
- Wolfire M. G., Tielens A. G. G. M., Hollenbach D., Kaufman M. J., 2008, *ApJ*, 680, 384
- Zemp, M., Gnedin, O. Y., Gnedin, N. Y., & Kravtsov, A. V. 2012, *ApJ*, 748, 54

gas is optically thin. For each spatial location, we only consider sources of radiation that lie within an oct, i.e. a collection of 8 cells at the highest level of refinement. Therefore the corresponding UV flux is:

$$G(t) = \frac{1}{G'_0} \alpha \frac{\sum_{i \in \text{oct}} L_{\text{LW}}(t - t_{s,i})}{4\pi \Delta x^2 \Delta \lambda c}, \quad (\text{A1})$$

where  $t$  is the time elapsed in the simulation,  $\Delta x$  is the size of a resolution element,  $c$  is the speed of light,  $\Delta \lambda = 1110 - 912 \text{ \AA}$  and  $G'_0 = 4 \times 10^{-17} \text{ erg cm}^{-3} \text{ \AA}^{-1}$ . The factor  $\alpha \simeq 2.876$  gives the correct average flux at the centre of a cell when stars are randomly distributed (with uniform density) within an oct. This coefficient has been measured with a Monte Carlo method. In our simulations,  $\Delta x \simeq 180 \text{ pc}$  and is comparable with the typical size of GMCs.

## APPENDIX A: INTERSTELLAR UV FIELD

Each star particle in our simulations represents a simple stellar population. We use the STARBURST99 templates (Leitherer et al. 1999) – with a Kroupa (2001) initial mass function (IMF) – to compute the luminosity in the LW band,  $L_{\text{LW}}(t_s)$ , as a function of stellar age,  $t_s$ . We then propagate this radiation up to a maximum distance assuming that the